Glucose-dependent glycosphingolipid biosynthesis fuels CD8$^+$ T cell function and tumor control

Joseph Longo[1], Lisa M. DeCamp[1], Brandon M. Oswald[1], Robert Teis[1], Alfredo Reyes-Oliveras[2], Michael S. Dahabieh[1], Abigail E. Ellis[3], Michael P. Vincent[3], Hannah Damico[4], Kristin L. Gallik[5], Shelby E. Compton[1], Colt D. Capan[3], Kelsey S. Williams[1,6], Corinne R. Esquibel[5], Zachary B. Madaj[4], Hyoungjoo Lee[3], Dominic G. Roy[7,8,9], Connie M. Krawczyk[1], Brian B. Haab[2], Ryan D. Sheldon[3], Russell G. Jones[1,6,*]

[1]Department of Metabolism and Nutritional Programming, Van Andel Institute, Grand Rapids, MI, USA

[2]Department of Cell Biology, Van Andel Institute, Grand Rapids, MI, USA

[3]Mass Spectrometry Core, Van Andel Institute, Grand Rapids, MI, USA

[4]Bioinformatics and Biostatistics Core, Van Andel Institute, Grand Rapids, MI, USA

[5]Optical Imaging Core, Van Andel Institute, Grand Rapids, MI, USA

[6]Metabolism and Nutrition Program, Van Andel Institute, Grand Rapids, MI, USA

[7]Centre de Recherche du Centre Hospitalier de l'Université de Montréal, Montréal, Canada

[8]Département de Microbiologie, Infectiologie et Immunologie, Université de Montréal, Montréal, Canada

[9]Institut du Cancer de Montréal, Montréal, Canada

*Corresponding author

Correspondence: Dr. Russell G. Jones, russell.jones@vai.org

SUMMARY

Glucose is essential for T cell proliferation and function, yet its specific metabolic roles *in vivo* remain poorly defined. Here, we identify glycosphingolipid (GSL) biosynthesis as a key pathway fueled by glucose that enables $CD8^+$ T cell expansion and cytotoxic function *in vivo*. Using ^{13}C-based stable isotope tracing, we demonstrate that $CD8^+$ effector T cells use glucose to synthesize uridine diphosphate-glucose (UDP-Glc), a precursor for glycogen, glycan, and GSL biosynthesis. Inhibiting GSL production by targeting the enzymes UGP2 or UGCG impairs $CD8^+$ T cell expansion and cytolytic activity without affecting glucose-dependent energy production. Mechanistically, we show that glucose-dependent GSL biosynthesis is required for plasma membrane lipid raft integrity and aggregation following TCR stimulation. Moreover, UGCG-deficient $CD8^+$ T cells display reduced granzyme expression and tumor control *in vivo*. Together, our data establish GSL biosynthesis as a critical metabolic fate of glucose—independent of energy production—required for $CD8^+$ T cell responses *in vivo*.

KEYWORDS

$CD8^+$ T cells, cytotoxic function, glucose, glycosphingolipids, immunometabolism, lipidomics, lipid rafts, nucleotide sugar metabolism, metabolomics, UGCG

INTRODUCTION

The adaptive immune system plays a critical role in host defense against infections and cancer. T cells are central players in the adaptive immune response and respond to antigen-specific signals by activating, proliferating, and differentiating into effector T cell subsets tailored to identify and eliminate threats to the host. Reprogramming of cellular metabolism is integral to T cell responses. Upon T cell receptor (TCR) engagement and appropriate co-stimulation, naïve T (Tn) cells dramatically alter their metabolic activity as they become activated and differentiate into effector T (Teff) cells[1–3]. This metabolic reprogramming is required to meet the increased metabolic demands of cell growth, proliferation, and effector function[1–3].

A critical step in the formation of functional Teff cells is the increased expression of glucose transporters at the plasma membrane and uptake of glucose from the extracellular environment[4–6]. T cells activated *in vitro* predominantly metabolize glucose via aerobic glycolysis and produce large amounts of lactate, a process known as the Warburg effect[7–9]. This shift towards increased glycolysis is critical, as restricting glucose availability or inhibiting glycolysis impairs T cell survival, proliferation, and cytokine production *in vitro*[4,7,10–13]. However, in addition to aerobic glycolysis, T cell activation also promotes an increase in oxidative phosphorylation (OXPHOS)[7,14], which can be fueled in part by glucose-derived pyruvate[9,15]. Interestingly, compared to *in vitro*-activated $CD8^+$ T cells, antigen-specific $CD8^+$ T cells activated *in vivo* display reduced lactate production and increased rates of OXPHOS[9]. Under physiologic conditions, however, $CD8^+$ T cells preferentially oxidize non-glucose carbon sources to fuel tricarboxylic acid (TCA) cycle metabolism and OXPHOS[15–17], and instead use glucose to support anabolic growth pathways such as nucleotide[9,15] and lipid[18] biosynthesis. Together, these studies indicate that $CD8^+$ T cells *in vivo* have distinct requirements for glucose other than energy production; however, the metabolic fates of glucose critical for supporting Teff cell responses under physiologic conditions remain poorly defined.

Here, we use *in vivo* ^{13}C-glucose tracing to track metabolic fates of glucose that are critical for effector function. We demonstrate that $CD8^+$ Teff cells responding to infection preferentially use glucose to synthesize the nucleotide sugar uridine diphosphate-glucose (UDP-Glc), a critical metabolic intermediate for glycogen, glycan, and glycosphingolipid (GSL) biosynthesis. We further demonstrate that inhibiting glucose-dependent UDP-Glc biosynthesis—by depleting the enzyme

UDP-Glc pyrophosphorylase 2 (UGP2)—significantly impairs T cell expansion in response to infection *in vivo*. Mechanistically, we demonstrate that glucose-derived UDP-Glc is required for *de novo* GSL biosynthesis. Moreover, inhibiting GSL production—by targeting UDP-Glc ceramide glucosyltransferase (UGCG)—impairs $CD8^+$ T cell expansion *in vivo* without affecting bioenergetics or energy production. This proliferative defect is associated with reduced accumulation of GSLs in the plasma membrane. GSLs are integral components of lipid rafts, microdomains at the plasma membrane that are required for optimal cell signaling. Blocking GSL biosynthesis by targeting UGCG expression impairs lipid raft aggregation following TCR stimulation. T cells with reduced glucose-dependent GSL biosynthesis display reduced granzyme expression, compromising $CD8^+$ T cell cytotoxic function and tumor control *in vivo*. Together, our data highlight GSL biosynthesis as an essential metabolic fate of glucose required to maintain membrane lipid raft integrity, $CD8^+$ T cell proliferation, and cytotoxic function *in vivo*.

RESULTS

UDP-Glc biosynthesis is a major metabolic fate of glucose in physiologically activated $CD8^+$ T cells

To delineate the metabolic fates of glucose in $CD8^+$ Teff cells *in vivo*, we employed a stable isotope infusion strategy developed and previously described by our group[9,19]. This approach uses $CD8^+$ OT-I cells expressing a transgenic TCR specific for ovalbumin (OVA) and the CD90.1 (Thy1.1) variant of CD90, enabling us to distinguish and rapidly isolate antigen-specific T cells from hosts. $Thy1.1^+CD8^+$ OT-I cells were adoptively transferred into $Thy1.2^+$ C57BL/6J hosts, which were subsequently infected with an attenuated strain of *Listeria monocytogenes* (*Lm*) expressing OVA (*Lm*-OVA) (**Figure 1A**). At the peak of infection (3 days post-infection (dpi)), either $CD8^+CD44^{low}$ Tn cells or antigen-specific ($Thy1.1^+$) Teff cells were isolated from spleens using magnetic beads, and analyzed immediately by liquid chromatography–mass spectrometry (LC-MS) (**Figure 1A**). $CD8^+$ T cells were isolated at 3 dpi to capture early metabolic changes displayed by actively proliferating Teff cells[17].

As expected with this infusion protocol[9,19], we achieved ~30% enrichment of ^{13}C-glucose m+6 in serum with ~10% or less enrichment of other glucose isotopologues (**Figure S1A**). The

greatest enrichment of ^{13}C-glucose-derived carbon in Tn cells was observed in glycolytic (lactate) and TCA cycle-derived (citrate, malate, aspartate) metabolites, as well as uridine diphosphate (UDP)-hexose (UDP-Hex) (**Figure 1B**). Interestingly, we observed similar enrichment of ^{13}C-glucose-derived carbon in the TCA cycle in activated Teff cells compared to Tn cells (**Figure 1B**). However, in contrast to Tn cells, Teff cells displayed a dramatic increase in ^{13}C-glucose-dependent synthesis of metabolites generated from early glycolytic intermediates, namely nucleotides, nucleotide sugars, and serine (**Figure 1B**). In particular, nucleotide sugars, including UDP-Hex and UDP-N-acetylglucosamine (UDP-GlcNAc), were extensively labeled from glucose, indicating that nucleotide sugar biosynthesis is a major fate of glucose metabolism in CD8$^+$ Teff cells.

To resolve the kinetics of glucose incorporation into nucleotide sugars relative to other glycolysis-derived metabolites (**Figure 1C**), CD8$^+$ OT-I cells were activated by *Lm*-OVA infection as in **Figure 1A**, but isolated and cultured *ex vivo* in a physiologic medium (i.e., VIM[15]) containing ^{13}C-glucose for up to 2 h. Cells were subjected to the same LC-MS method as in **Figure 1B**, as well as a high-pH hydrophilic interaction chromatography (HILIC) LC-MS method to better resolve different UDP-Hex species. Similar to *in vivo*-labeled CD8$^+$ Teff cells, *Lm*-OVA-activated CD8$^+$ Teff cells exposed to ^{13}C-glucose *ex vivo* displayed ^{13}C enrichment in UTP, serine, and UDP-GlcNAc, but with varying kinetics (**Figure 1D**). Strikingly, the most rapid ^{13}C labeling in *Lm*-OVA-activated CD8$^+$ Teff cells was seen in the nucleotide sugar UDP-glucose (UDP-Glc), with >50% of the UDP-Glc pool labeled from glucose within 15 min and ~100% of the UDP-Glc pool labeled by 30 min (**Figure 1D**). Consistent with the rapid labeling of UDP-Glc from ^{13}C-glucose, the total UDP-Glc pool was ~6-fold greater in Teff cells compared to Tn cells at 3 dpi (**Figure 1E**). UDP-Glc-derived metabolites including UDP-galactose (UDP-Gal) and UDP-glucuronic acid (UDP-GlcA) were also rapidly labeled from ^{13}C-glucose *ex vivo*, with kinetics of UDP-Gal labeling similar to that of UDP-Glc (**Figure S1B**).

UDP-Glc is synthesized from glucose-1-phosphate (Glc-1-P) and UTP, both of which can be derived from ^{13}C-glucose (**Figure 1F**). A fully labeled glucose molecule ([U-^{13}C]-glucose) can generate UDP-Glc m+6 from Glc-1-P, while glucose metabolized via the pentose phosphate pathway (PPP) will generate ribose m+5 and subsequently UTP m+5 (**Figures 1C** and **S1C-D**). Finally, glucose-derived aspartate can also contribute carbon to the nitrogenous base of UTP, resulting in an additional 2-3 ^{13}C-labeled carbons (to generate UTP m+7 or m+8) depending on

whether glucose-derived pyruvate enters the TCA cycle via pyruvate dehydrogenase (m+2) or pyruvate carboxylase (m+3) (**Figure S1D**). Isotopologue distribution analysis of UDP-Glc production in *Lm*-OVA-activated CD8$^+$ Teff cells over time revealed an early increase in UDP-Glc m+6, followed by increased proportions of UDP-Glc m+11 and m+13 isotopologues by 2 h (**Figure 1G**). This labeling patten suggests that glucose-derived Glc-1-P is used first to synthesize UDP-Glc, and then m+5 UTP (labeled ribose sugar) and m+7 UTP (labeled ribose sugar and nitrogenous base) increasingly contribute to UDP-Glc synthesis over time. Importantly, the rapid synthesis of UDP-Glc in CD8$^+$ Teff cells is not specific to *Lm*-OVA infection, as both murine and human CD8$^+$ T cells activated *in vitro* with anti-CD3 and anti-CD28 antibodies similarly use glucose to synthesize UDP-Glc (**Figure 1H**). Collectively, these data reveal UDP-Glc biosynthesis as a major fate of glucose metabolism in CD8$^+$ Teff cells, and that rapid synthesis of UDP-Glc is coordinated by sourcing carbon from multiple glucose-derived metabolic pathways in CD8$^+$ Teff cells.

UGP2 coordinates UDP-Glc biosynthesis in T cells to maintain T cell homeostasis and fuel CD8$^+$ Teff responses to infection

Despite UDP-Glc being a major fate of glucose in Teff cells, the contribution of UDP-Glc metabolism to CD8$^+$ T cell function is unknown. To test the importance of this pathway to T cell function *in vivo,* we generated *Ugp2*-floxed (*Ugp2*$^{fl/fl}$) mice and crossed them with the *Cd4-Cre* transgenic mice to generate a mouse model with conditional deletion of *Ugp2* in mature T cells (**Figure 2A**). Baseline immunophenotyping of *Ugp2*$^{fl/fl}$*Cd4-Cre* mice revealed a significant reduction in peripheral CD3$^+$ T cells compared to *Cd4-Cre*-negative control littermates, irrespective of sex (**Figures 2B-C**). Within the CD3$^+$ T cell subset, we observed a slight reduction in the percentage of CD4$^+$ and CD8$^+$ T cells, which translated to a 5-6-fold reduction in the total number of mature CD4$^+$ and CD8$^+$ T cells in the periphery (**Figures 2D-F**). Splenic B cell and NK cell numbers were similar between genotypes (**Figure S2A**).

To identify whether the decrease in peripheral T cells was due to impaired T cell development, we profiled T cell subsets in the thymus. Interestingly, we observed no difference in the percentage or number of CD4 and CD8 double-negative, double-positive, or single-positive T cells in the thymus (**Figure S2B-C**). Taken together, these data suggest that UGP2 is required for

T cell homeostasis outside the thymus. Notably, mature CD3$^+$ T cells isolated from the spleen of *Ugp2*$^{fl/fl}$*Cd4-Cre* mice retained UGP2 protein expression (**Figure S2D**) and the abundance of UDP-Glc in T cells from *Ugp2*$^{fl/fl}$*Cd4-Cre* mice was similar to control cells (**Figure S2E**). These data suggest that UPG2 is essential for peripheral T cell homeostasis and that the remaining mature T cells in *Ugp2*$^{fl/fl}$*Cd4-Cre* mice escaped *Ugp2* gene deletion.

Given that UGP2 appears to be essential for mature peripheral T cell homeostasis, we silenced *Ugp2* in purified, *in vitro*-activated CD8$^+$ T cells using a short hairpin RNA (shRNA) as an alternative strategy. Compared to a control shRNA targeting firefly luciferase (shCtrl), expression of a *Ugp2*-targeting shRNA (sh*Ugp2*) reduced UGP2 protein expression in CD8$^+$ T cells (**Figure 2G**) and ablated both total and ^{13}C-glucose-derived UDP-Glc pools (**Figures 2H-I**). Interestingly, the distribution of ^{13}C-glucose-derived UDP-Glc isotopologues in sh*Ugp2*-expressing CD8$^+$ T cells was similar to control cells (**Figure S2F**), indicating that this strategy reduced the overall rate of UDP-Glc synthesis rather than changing its source of production.

We next examined the impact of silencing UGP2 on CD8$^+$ T cell function. Knockdown of *Ugp2* in activated CD8$^+$ T cells did not dramatically compromise cell proliferation *in vitro* (**Figure 2J**), nor did it alter markers of T cell activation (**Figure S2G**). However, reducing UGP2-dependent glucose metabolism had a dramatic impact on Teff cell expansion *in vivo*. We adoptively transferred shCtrl- or sh*Ugp2*-expressing Thy1.1$^+$CD8$^+$ OT-I cells into Thy1.2$^+$ hosts, and then infected the mice with *Lm*-OVA the following day (**Figure 2K**)[9,15]. We observed a significant reduction in the percentage of antigen-specific (Thy1.1$^+$) sh*Ugp2*-expressing CD8$^+$ Teff cells at the peak of infection (7 dpi), which translated to a ~2.5-fold decrease in the total number of antigen-specific cells compared to controls (**Figures 2L-M**). Despite this reduction in antigen-specific CD8$^+$ T cell expansion, UGP2-depleted cells displayed no major defects in their ability to produce cytokines or differentiate into effector or memory precursor subsets (**Figures 2M-N** and **S2H-K**). Thus, our data indicate that UGP2, despite having minimal impact on CD8$^+$ T cell proliferation or survival *in vitro*, is critical for both T cell homeostasis and expansion in response to infection *in vivo*.

UDP-Glc fuels glycogen and glycan biosynthesis in CD8⁺ T cells

We next sought out to identify the metabolic pathway(s) downstream of UDP-Glc biosynthesis required for CD8⁺ Teff cell responses *in vivo*. UDP-Glc is a central intermediate for the synthesis of several metabolites, including glycogen, UDP-Gal, glycans, glycosaminoglycans, and GSLs (**Figure 3A**). Glycogen is a glucose polysaccharide that serves as a form of carbon storage in animals. A previous study reported that glycogen pools are elevated in CD8⁺ memory T (Tmem) cells compared to Tn and Teff cells, and that glycogen storage is required for the formation of T cell memory[20]. Concordantly, impairing glycogen mobilization has been shown to impair CD8⁺ Tmem cell responses *in vivo*, while having no effect on primary Teff cell responses following *Lm*-OVA infection[21,22]. We observed a significant decrease in glycogen pools in sh*Ugp2*-expressing CD8⁺ T cells compared to controls (**Figure 3B**); however, since we also found that UGP2 depletion significantly impairs CD8⁺ Teff cell expansion following *Lm*-OVA infection (**Figures 2L-M**), we decided to quantify other UDP-Glc-derived metabolites in sh*Ugp2*-expressing CD8⁺ T cells.

Metabolomics analysis of control and sh*Ugp2*-expressing CD8⁺ T cells revealed a significant decrease in the pool of UDP-Gal in UGP2-depleted cells, while the pool of UDP-GlcA, a precursor for glycosaminoglycan biosynthesis, was similar between control and sh*Ugp2*-expressing cells (**Figure 3C**). UDP-Gal serves as a substrate for β-1,4-galactosyltransferases (B4GALTs), which catalyze the synthesis of glycoproteins and glycolipids[23,24]. While evidence for functional redundancies between B4GALT enzymes exists[23,24], B4GALT1 primarily catalyzes the transfer of Gal to terminal GlcNAc acceptors on complex-type N-glycans[25], whereas B4GALT5/6 catalyze UDP-Gal-dependent synthesis of lactosylceramide (LacCer) and GSLs[26,27] (**Figure 3A**). In addition to UDP-Gal-dependent galactosylation of glycoproteins, UDP-Glc can also regulate glycoprotein folding and N-glycan initiation at the endoplasmic reticulum[28,29]. To interrogate whether silencing *Ugp2* in CD8⁺ T cells impacted protein N-glycosylation, we probed cells with the mannose-binding lectin Concanavalin A (ConA), which is commonly used to detect N-glycans at the cell surface[30]. Surprisingly, we observed a slight, statistically significant increase in the mean fluorescence intensity (MFI) of ConA on sh*Ugp2*-expressing CD8⁺ T cells (**Figure 3D**), indicating that UGP2-depleted cells either have a greater number of N-glycans on their surface or an altered N-glycan composition that favors ConA binding.

N-glycans undergo maturation in the Golgi apparatus, where B4GALT1 transfers Gal from UDP-Gal to terminal GlcNAc acceptors to form N-acetyllactosamine (LacNAc) and initiate N-glycan extension[31] (**Figure 3E**). To further interrogate the phenotype of N-glycans in sh*Ugp2*-expressing $CD8^+$ T cells, we probed cells with a panel of lectins that recognize different N-glycan features. Interestingly, sh*Ugp2*-expressing $CD8^+$ T cells displayed a significant increase in terminal GlcNAc and a decrease in terminal Gal as determined by binding of *Bandeiraea simplicifolia* lectin (BSL) II and BSL I, respectively (**Figure 3E**). Moreover, we observed a decrease in poly-LacNAc features in sh*Ugp2*-expressing $CD8^+$ T cells, as evidenced by reduced MFI of *Datura stramonium* lectin (DSL) (**Figure 3E**). Taken together, these data indicate that blocking glucose-dependent UDP-Gal production (via UGP2 depletion) impairs N-glycan extension.

Consistent with the increase in ConA binding to UGP2-depleted $CD8^+$ T cells (**Figure 3D**), we also observed a slight but significant increase in binding of another mannose-binding lectin, *Galanthus nivalis* lectin (GNL), in UGP2-depleted cells (**Figure 3E**). Without proper N-glycan extension, the mannose residues in the core of the truncated N-glycans (**Figure 3E**) may become more exposed to mannose-binding lectins like ConA and GNL. Indeed, these lectins typically exhibit lower affinity for core mannose residues when additional carbohydrate modifications, such as branch extensions, are present[32,33]. Hence, silencing *Ugp2* and disrupting glucose-dependent UDP-Gal biosynthesis remodels the composition of the glycocalyx—glycan coating on the cell surface—of $CD8^+$ T cells.

UGP2 is required for GSL biosynthesis in $CD8^+$ T cells

In addition to their roles in N-glycosylation, UDP-Glc and UDP-Gal are also substrates for GSL biosynthesis (**Figure 3A**). The enzyme UGCG catalyzes the first step in GSL biosynthesis by transferring Glc from UDP-Glc to a ceramide molecule to produce glucosylceramide (GlcCer) (**Figure 3A**). B4GALT5 then transfers Gal from UDP-Gal to GlcCer to produce LacCer, which goes on to produce a wide array of GSLs including gangliosides[26,27,34]. To determine how depleting UGP2 impacted GSL synthesis, we conducted lipidomics analysis of control and sh*Ugp2*-expressing $CD8^+$ T cells. The most robust change we observed was a decrease in numerous hexosylceramide (HexCer) and GA1 ganglioside species in sh*Ugp2*-expressing T cells (**Figures 3F-**

G and **S3A-B**). This decrease in HexCer and ganglioside species was accompanied by a slight increase in ceramides and ceramide-derived sphingomyelins (**Figure 3F**), suggesting a re-routing of ceramides from HexCer biosynthesis towards alternative lipid metabolic pathways when UGP2 is depleted. Notably, depletion of UDP-Glc and GSL pools in UGP2-depleted $CD8^+$ T cells had little-to-no impact on the abundance or ^{13}C labeling of other glucose-derived metabolites linked to T cell proliferation, including adenosine triphosphate (ATP), serine, UDP-GlcNAc, and citrate (**Figure S3C-D**). Collectively, these data indicate that UGP2 regulates the production of multiple UDP-Gal-dependent metabolic processes in $CD8^+$ T cells, without impacting other glucose-dependent biosynthetic and bioenergetic pathways.

$CD8^+$ Teff cells direct glucose to fuel GSL biosynthesis in vivo

To identify how UDP-Gal-dependent metabolic pathways change with T cell activation, we mined previously published proteomics data from $CD8^+$ Tn and Teff cells isolated from *Lm*-OVA-infected mice[9]. Relative to Tn cells, $CD8^+$ Teff cells at 3 dpi displayed increased expression of the enzyme UDP-Gal-4-epimerase (GALE) (**Figure 4A**), which catalyzes the conversion of UDP-Glc to UDP-Gal (**Figures 3A**). This upregulation of GALE expression with T cell activation is consistent with the robust glucose-dependent synthesis of UDP-Gal observed in activated $CD8^+$ T cells (**Figure S1B**). Teff cells also displayed higher expression of UGCG and B4GALT5 relative to Tn cells, while the expression of B4GALT1, which directs UDP-Gal to protein N-glycosylation, was similar between Teff and Tn cells (**Figure 4A**). Taken together, these data indicate metabolic reprogramming in activated $CD8^+$ T cells directs glucose towards increased GSL biosynthesis *in vivo*.

To directly test whether $CD8^+$ Teff cells actively direct glucose into GSL biosynthesis *in vivo*, we repeated the ^{13}C-glucose *in vivo* infusion experiment in *Lm*-OVA-infected mice as described in **Figure 1A**, and quantified the abundance and ^{13}C labeling of GSLs in purified Tn and Teff cells by LC-MS. The overall contribution of ^{13}C-glucose to HexCer and GA1 ganglioside synthesis was significantly increased in $CD8^+$ Teff cells at 3 dpi compared to Tn cells (**Figure 4B**). Strikingly, we observed a ~20% relative enrichment of m+6-labeled HexCer species (i.e., d18:1/16:0, d18:1/24:1, d18:2/24:1) in $CD8^+$ Teff cells after only 2 h of ^{13}C-glucose infusion, indicating rapid turnover of these lipid pools. Teff cells had higher amounts of both total and ^{13}C-glucose-derived

HexCer and GA1 ganglioside pools compared to Tn cells, further supporting the upregulation of GSL biosynthesis in physiologically activated $CD8^+$ T cells *in vivo* (**Figures 4C-E**). GA1 gangliosides are synthesized via the sequential addition of carbohydrates to GlcCer to produce a molecule comprised of a ceramide and four-sugar chain (**Figure 4D**). After 2 h of ^{13}C-glucose infusion, $CD8^+$ Teff cells had predominantly m+6-labeled GA1 ganglioside (one labeled sugar); however, m+12- and m+18-labeled GA1 gangliosides were also observed, suggesting that glucose contributes to the synthesis of multiple nucleotide sugars used to synthesize GA1 gangliosides (**Figure 4E**). Notably, proliferating human $CD8^+$ T cells also directed glucose into GSL biosynthesis; however, GM3 was the predominant ganglioside species detected in human T cells (**Figure S4**), suggesting some level of species-dependent regulation of this metabolic pathway. Taken together, these data not only reveal that $CD8^+$ Teff cells use glucose to synthesize GSLs *in vivo*, but that—due to the high turnover rate of these lipids—Teff cells actively use glucose to maintain synthesis of these lipids.

Glucose-dependent GSL biosynthesis is essential for T cell expansion in vivo

To determine the contribution of glucose-dependent GSL biosynthesis to $CD8^+$ Teff cell responses *in vivo*, we targeted the enzyme UGCG, which catalyzes the first glycosylation step in GSL biosynthesis (**Figure 3A**). We first took a pharmacological approach to inhibit UGCG enzymatic activity using the drug eliglustat[35] (**Figure 5A**). Treating $CD8^+$ T cells with a range of eliglustat concentrations (0-25 μM) during *in vitro* anti-CD3 and anti-CD28 antibody stimulation resulted in a dose-dependent decrease in cell proliferation (**Figures 5B**). At 4 μM (IC_{50} for proliferation), eliglustat significantly decreased the abundance of both HexCer and GA1 ganglioside pools (**Figure 5C**). Similarly, treating activated $CD8^+$ T cells with eliglustat reduced cell proliferation in a concentration-dependent manner, with no effect on cell viability at concentrations $\leq$ 4 μM (**Figures S5A-B**).

We validated these findings using a single guide RNA (sgRNA) targeting *Ugcg*, which ablated UGCG protein expression (**Figures 5D** and **S5C**) and significantly reduced both GSL abundance and ^{13}C-glucose-dependent GSL biosynthesis in $CD8^+$ T cells (**Figures 5E-F**). Importantly, deletion of *Ugcg* did not significantly affect glycolysis or total ATP production, as

evidenced by similar extracellular acidification and oxygen consumption rates (**Figure 5G**) and basal ATP production rates (**Figure 5H**) between control and UGCG-deficient CD8$^+$ T cells. While we observed a slight decrease in basal ATP production from glycolysis in UGCG-deficient CD8$^+$ T cells (**Figure 5H**), total ATP production was preserved due to a compensatory increase in ATP production from OXPHOS (**Figures 5G-H**). Furthermore, unlike with *Ugp2* silencing in CD8$^+$ T cells, both glycogen pools and UDP-Gal-dependent N-glycan extension were unaffected by *Ugcg* deletion (**Figure S5D-E**). Despite having no effects on ATP production, glycogen levels, or UDP-Gal-dependent N-glycan extension, deleting *Ugcg* reduced the proliferation of CD8$^+$ T cells *in vitro* (**Figure 5I**), similar to our observations with eliglustat treatment (**Figure 5B**). Moreover, similar to UGP2 depletion (**Figures 2L-M**), *Ugcg* deletion significantly reduced the number of antigen-specific CD8$^+$ Teff cells *in vivo* at 7 dpi following *Lm*-OVA infection (**Figures 5J-K**), without compromising cytokine production (**Figures S5F-H**) or cell differentiation (**Figures S5I-J**). Together, these data indicate that GSL biosynthesis—regulated by the enzyme UGCG—is the key fate of glucose downstream of UGP2-mediated UDP-Glc production that is critical for CD8$^+$ Teff cell expansion *in vivo*.

GSL biosynthesis is required to maintain lipid rafts at the plasma membrane

To determine the downstream consequences of *Ugcg* deletion in CD8$^+$ T cells, we performed global proteomic analysis of control and UGCG-deficient CD8$^+$ T cells. We identified 37 proteins that were significantly upregulated in UGCG-deficient CD8$^+$ T cells and 59 proteins that were significantly downregulated (**Figure 6A** and **Table S1**). Gene set enrichment analysis (GSEA) revealed several pathways influenced by UGCG expression (**Figures 6B** and **S6**, and **Table S2**). Notably, pathways related to TCR signal transduction and immune synapse formation, including "positive regulation of leukocyte degranulation" and "actin filament bundle assembly", were downregulated in UGCG-deficient CD8$^+$ T cells (**Figure 6B** and **Table S2**). In particular, protein expression of several granzyme family members (GZME, GZMK, GZMA) and perforin (PRF1) were significantly decreased in UGCG-deficient CD8$^+$ T cells, as well as proteins implicated in actin remodeling and intracellular trafficking (ARL6, SCIN, SWAP70) (**Figure 6A**).

GSLs, particularly gangliosides, are integral components of lipid rafts, which are lipid-rich microdomains at the plasma membrane that serve as platforms for cell signaling[36]. In T cells, stimulation of the TCR is followed by aggregation of lipid rafts, which brings together key proteins involved in TCR signal transduction[37]. Importantly, lipid raft defects have been associated with compromised T cell proliferation[38]. Hence, we explored lipid raft aggregation as a putative mechanism for the reduced cell proliferation triggered by loss of glucose-dependent GSL biosynthesis (**Figure 5**). To determine the impact of *Ugp2* silencing or *Ugcg* deletion on lipid rafts in $CD8^+$ T cells, we took advantage of the cholera toxin B subunit (CTxB), which binds GM1 and other gangliosides and is used to measure lipid rafts at the cell surface[39,40]. Indeed, both UGP2-depleted and UGCG-deficient $CD8^+$ T cells displayed a reduction in the MFI of CTxB, indicating reduced levels of lipid rafts at the plasma membrane (**Figures 6C-D**). Moreover, while TCR crosslinking resulted in lipid raft aggregation in control cells, UGCG-deficient $CD8^+$ T cells displayed impaired lipid raft aggregation (**Figure 6E**). Together, these data indicate that glucose-dependent GSL biosynthesis is required to maintain the ganglioside composition of lipid rafts in T cells.

UGCG controls CD8⁺ T cell cytotoxic function and anti-tumor immunity

Given the decrease in cytotoxic factors and lipid raft defects in UGCG-deficient $CD8^+$ T cells (**Figure 6A-B**), we evaluated the role of glucose-dependent GSL biosynthesis in T cell-mediated tumor control. First, we evaluated the cytolytic capacity of UGCG-deficient $CD8^+$ T cells. Control or UGCG-deficient $Thy1.1^+CD8^+$ OT-I cells were transferred into $Thy1.2^+$ C57BL/6J hosts, infected with *Lm*-OVA, and the cytotoxic activity of antigen-specific OT-I cells isolated from infected animals at 7 dpi was assessed via T cell killing assay using OVA-expressing MC38 (MC38-OVA) colon cancer cells as targets[16]. UGCG-deficient OT-I cells were impaired in their ability to lyse cancer cells, with ~6x the number of UGCG-deficient cells required to kill the same number of cancer cells as control OT-I cells (**Figure 7A**). Moreover, at a fixed effector:target ratio, UGCG-deficient OT-I cells displayed a reduced rate of T cell killing (**Figure 7B**). Consistent with our proteomics analysis (**Figure 6A-B**) and the reduced killing capacity of UGCG-deficient $CD8^+$ T cells (**Figure 7A-B**), physiologically activated UGCG-deficient $CD8^+$ OT-I cells had lower Granzyme B (GZMB) expression *ex vivo* (**Figure**

7C). Thus, in addition to proliferative defects, $CD8^+$ T cells unable to maintain GSL production from glucose display impaired cytotoxic function.

Finally, to test whether cytotoxic defects linked to impaired GSL biosynthesis impact anti-tumor immunity, we adoptively transferred control or UGCG-deficient $Thy1.1^+CD8^+$ OT-I cells into B16-OVA tumor-bearing mice and measured tumor growth over time. While transfer of control OT-I cells significantly delayed tumor growth and prolonged overall survival, animals that received UGCG-deficient OT-I cells displayed similar tumor growth as mice that received no OT-I cells (**Figure 7D-E**). Unlike the *Lm*-OVA infection model (**Figure 5I-J**), the defect in tumor control conferred by UGCG-deficient $CD8^+$ T cells was not due to a reduction in the percentage of antigen-specific $CD8^+$ T cells in the tumor (**Figure 7F**). Rather, we observed a significant reduction in GZMB expression in antigen-specific, UGCG-deficient tumor-infiltrating lymphocytes (TILs) (**Figure 7G**). Collectively, our data indicate that glucose-dependent GSL biosynthesis is required for optimal $CD8^+$ T cell cytotoxic function and effective tumor control.

DISCUSSION

Glucose is an essential substrate for T cell proliferation and function. While glucose is a prominent bioenergetic substrate for ATP production in most cell types, it has become increasingly clear that energy production is not the only metabolic fate for glucose important for T cell responses *in vivo*. Here, we show that nucleotide sugar biosynthesis—specifically the production of UDP-Glc—is an essential fate for glucose in proliferating $CD8^+$ Teff cells independent of energy production. The rapid production of UDP-Glc from glucose is a feature of both mouse and human $CD8^+$ T cells and requires the coordination of multiple glucose-fueled anabolic pathways (i.e., PPP, nucleotide biosynthesis, aspartate biosynthesis) for optimal production. Glucose-dependent UDP-Glc biosynthesis is critical for both quiescent T cell homeostasis and Teff cell expansion. Conditional deletion of *Ugp2* in T cells does not notably affect thymic development, but significantly depletes mature T cell populations in the periphery. Concordantly, preventing the conversion of glucose to UDP-Glc by depleting UGP2 in activated $CD8^+$ T cells cripples their ability to respond to *Lm*-OVA infection *in vivo*. Importantly, blocking UDP-Glc biosynthesis did not affect the contribution of glucose to serine or nucleotide biosynthesis, which we previously showed are important for T cell

expansion[9,41], nor did it impair TCA cycle metabolism. While UDP-Glc is a substrate for several metabolic pathways, we found that blocking GSL biosynthesis (via UGCG inhibition) was sufficient to phenocopy the defects we observed with UGP2 depletion, implicating GSL biosynthesis as the key metabolic fate of glucose critical for optimal $CD8^+$ Teff cell responses. Mechanistically, glucose-dependent GSL biosynthesis is essential for maintaining membrane lipid raft integrity, and disrupting this pathway led to reduced $CD8^+$ T cell cytotoxicity and poor tumor control. Taken together, our results establish glucose-dependent GSL biosynthesis as an essential metabolic pathway in $CD8^+$ T cells that is independent of other known biosynthetic and bioenergetic fates of glucose.

Contrary to current models, our findings suggest that glucose functions predominantly as a biosynthetic precursor, rather than a bioenergetic substrate, in $CD8^+$ T cells under physiologic conditions. This is supported by recent evidence demonstrating that, under physiologic conditions, increased TCA cycle metabolism and oxidative ATP production by activated T cells is fueled by other, non-glucose carbon sources, including glutamine[15,17], lactate[15], acetate[17,42,43], and ketone bodies[15,16,44]. In the absence of these non-glucose carbon sources (i.e., *in vitro* cell culture), excess glucose can be used by proliferating $CD8^+$ T cells as both a biosynthetic and bioenergetic substrate. However, under physiologic conditions where these other carbon sources are abundant[45–47], glucose is spared from entering the TCA cycle and instead can feed biosynthetic pathways that generate other metabolites needed for cell proliferation, including serine[9,41], nucleotides[9,17,41], and UDP-GlcNAc[48]. Notably, these glucose-dependent metabolic pathways all converge on the synthesis of GSLs, which we show here are essential for $CD8^+$ Teff cell expansion and cytotoxic function. After only 2 h of ^{13}C-glucose infusion in *Listeria*-infected mice, almost 20% of the HexCer pools in activated $CD8^+$ Teff cells were labeled from ^{13}C-glucose, indicating rapid turnover of these lipid pools *in vivo*. Depleting GSL pools in activated T cells (via UGCG deletion) led to a loss of lipid raft integrity at the plasma membrane. Thus, sparing glucose from being metabolized for ATP production allows proliferating T cells to direct glucose towards GSL synthesis *in vivo* and maintain these essential lipid pools. We posit that the metabolic processes that fuel *in vivo* $CD8^+$ Teff cell activation, proliferation, and function are partitioned, whereby glutamine and other physiologic carbon sources such as ketone bodies are preferentially oxidized via the

TCA cycle to fuel T cell bioenergetics, which spares glucose to fuel biosynthetic pathways that branch from glycolysis, such as nucleotide, glycan, and GSL biosynthesis. How glucose-dependent GSL biosynthesis changes over the course of an immune response and whether GSLs contribute to T cell homeostasis during quiescent cell states remains to be determined.

Glycobiology remains an important but poorly understood area of immunology, due in part to the complex structures and biosynthesis of glycans, and the wide range of biological processes they regulate. T cell activation is associated with dramatic glycocalyx remodeling[49,50], which has implications for both T cell activation and function[51–53]. Our data reveal that a major fate of glucose in both mouse and human activated $CD8^+$ T cells is the rapid biosynthesis of nucleotide sugars required for glycosylation reactions, including UDP-GlcNAc and UDP-Glc. We show that inhibiting UDP-Glc biosynthesis via UGP2 depletion blunts N-glycan extension and impairs GSL biosynthesis, implicating UGP2 as a central regulator of the glycocalyx in $CD8^+$ T cells. In the present study, we focused primarily on the role of UDP-Glc in GSL biosynthesis. We demonstrated, for the first time, that $CD8^+$ Teff cells actively synthesize GSLs from glucose *in vivo* in response to pathogen challenge. In particular, we observed increased pools and ^{13}C-glucose labeling of asialo-series (i.e., GA1) gangliosides in proliferating Teff cells compared to resting Tn cells. This observation is consistent with a previous study that found mouse $CD8^+$ T cells predominantly express asialo-series gangliosides, whereas mouse $CD4^+$ T cells express a-series gangliosides (e.g., GM3-derived GM2)[54]. Interestingly, in human $CD8^+$ T cells, we detected glucose-derived GM3 rather than GA1 gangliosides, suggesting that while both mouse and human activated $CD8^+$ T cells synthesize GSLs, the types of GSLs produced may be species-dependent. Concordantly, a recent comprehensive indexing of glycan structures in activated mouse and human T cells revealed that increased glycan biosynthesis is a common feature of T cell activation, but the specific glycan structures expressed in mouse and human T cells differed due to divergent expression of multiple glycosyltransferase enzymes[55]. Species-dependent differences in glycan synthesis may explain key differences in immune responses observed across species.

A key consequence of inhibiting GSL biosynthesis in $CD8^+$ T cells (via UGP2 depletion or UGCG deletion) was a reduction in ganglioside-rich lipid rafts at the plasma membrane. We further showed that lipid raft aggregation following TCR crosslinking is compromised in UGCG-

deficient $CD8^+$ T cells. Lipids rafts have been implicated in T cell proliferation[54], polarization and migration[56], responsiveness to cytokines[57], and formation of the cytotoxic immunological synapse[58]. We therefore propose a model whereby glucose-dependent GSL biosynthesis tethers nutrient availability to the maintenance of signaling complexes at the plasma membrane, ensuring T cell proliferation and cytotoxic function are supported by sufficient glucose levels. This model is supported by our proteomics data, which showed reduced expression of granzymes and proteins involved in actin cytoskeleton organization in UGCG-deficient $CD8^+$ T cells. Moreover, lipid rafts have been reported to control naïve $CD8^+$ T cell homeostasis through tonic TCR signaling[57], and therefore a defect in lipid rafts could explain the reduced number of peripheral T cells we observed in *Ugp2*$^{fl/fl}$*Cd4-Cre* mice. Data from multiple different cell types, including the data we present here, show that inhibiting GSL biosynthesis *in vitro* impairs cell proliferation, but has little effect on cell viability[59,60]; however, *in vivo*, GSLs are key mediators of cell-cell and cell-environment communication, which are important for coordinating complex biological processes including embryonic development[60] and immune responses[54]. In addition to their structural contribution to lipid rafts, membrane GSLs may also regulate cell signaling and cell-cell adhesion via carbohydrate-carbohydrate interactions[55].

Glucose-dependent GSL biosynthesis has emerged as a key metabolic feature of tumor cells. For example, in oncogenic KRAS-driven pancreatic cancer cells, glucose-dependent GSL biosynthesis regulates KRAS plasma membrane localization and signaling[61]. Other studies show that cancer cell-intrinsic GSL biosynthesis promotes tumor growth by mediating immune evasion, and that inhibiting GSL biosynthesis in cancer cells increases cancer cell sensitivity to IFN-γ-induced growth arrest[62] and improves antigen presentation to cytotoxic $CD8^+$ T cells[63]. In this vein, eliglustat treatment may synergize with immune checkpoint blockade therapy to inhibit tumor growth[62,63]. Here, our findings suggest that systemic treatments that target UGCG, such as eliglustat, may compromise the cytotoxic capacity of $CD8^+$ T cells and hinder their ability to control tumor growth. Hence, while short-term eliglustat treatment may reduce tumor burden by inhibiting cancer cell-intrinsic GSL biosynthesis, prolonged treatment may have unintended consequences for long-term anti-tumor immunity. By contrast, immunometabolic modulation of

GSL biosynthesis may prove effective in modulating pathology in diseases driven by pathogenic T cells, such as autoimmune diseases.

LIMITATIONS OF THE STUDY

Given that deletion of *Ugp2* during T cell development was detrimental to T cell homeostasis and that surviving peripheral T cells still expressed UGP2, we were unable to study how disrupting glucose-dependent UDP-Glc and GSL biosynthesis affects the transition from the Tn to Teff cell state. We instead focused on studying how these metabolic pathways impact proliferating Teff cells *in vivo*. Inducible *Ugp2* or *Ugcg* deletion models will enable the study of GSL metabolism during different T cell state transitions in the future. Our data establish that glucose is used by $CD8^+$ T cells to sustain GSL biosynthesis during an immune response; however, further research is required to determine how different GSLs expressed at the plasma membrane of T cells interact with other membrane components on the same cell or neighboring cells to coordinate T cell responses.

ACKNOWLEDGMENTS

We thank Dr. Jim Dennis and members of the Jones and Krawczyk laboratories for scientific discussions contributing to this manuscript. We thank Jade Desjardins, Mitra Cowan, and the McGill Integrated Core for Animal Modeling for generating the *Ugp2*-floxed mouse model. We thank Jeanie Wedberg and Margene Brewer for administrative assistance. We thank members of the Van Andel Institute (VAI) Core Facilities for technical assistance, including Mass Spectrometry (RRID: SCR_024903), Flow Cytometry (RRID: SCR_022685), Bioinformatics and Biostatistics (RRID: SCR_024762), Vivarium (RRID: SCR_023211), Pathology and Biorepository (RRID: SCR_022912) and Optical Imaging (RRID: SCR_021968). We especially thank Christine Isaguirre and Molly Hopper (Mass Spectrometry), Rachael Sheridan (Flow Cytometry), Lisa Turner (Pathology and Biorepository), and Lorna Cohen (Optical Imaging) for their technical support. J.L. is supported by a VAI Metabolism & Nutrition (MeNu) Program Pathway-to-Independence Award and Canadian Institutes of Health Research (CIHR) Fellowship (MFE-181903). M.S.D. is supported by a VAI MeNu Program Pathway-to-Independence Award, Fonds de recherche du Québec-Santé (FRQS)

Postdoctoral Fellowship (0000289124), and CIHR Fellowship (MFE-403514). C.M.K. is supported by the National Institute of Allergy and Infectious Diseases (NIAID, R21AI153997) and VAI. B.B.H. is supported by VAI. R.G.J. is supported by the Paul G. Allen Frontiers Group Distinguished Investigator Program, Chan Zuckerberg Initiative (CZI), NIAID (R01AI165722), and VAI.

AUTHOR CONTRIBUTIONS

Conceptualization, J.L. and R.G.J.; Experimental Design, J.L., B.M.O., A.R-O., K.L.G., C.R.E., C.M.K., R.D.S., and R.G.J.; Investigation, J.L., L.M.D., B.M.O., R.T., A.R-O., M.S.D., A.E.E., S.E.C., and H.L.; Resources, D.G.R.; Data Analysis, J.L., R.T., A.R-O., A.E.E., M.P.V., H.D., K.L.G., C.D.C., Z.B.M., H.L., R.D.S., and R.G.J.; Writing, J.L. and R.G.J.; Visualization, J.L. and K.S.W.; Supervision, C.R.E., B.B.H., R.D.S., and R.G.J.; Funding Acquisition, R.G.J.

DECLARATION OF INTERESTS

R.G.J. is a scientific advisor to Servier Pharmaceuticals and is a member of the Scientific Advisory Board of Immunomet Therapeutics.

FIGURE LEGENDS

Figure 1: UDP-Glc biosynthesis is a major metabolic fate of glucose in physiologically activated CD8$^+$ T cells.

(**A**) Experimental setup for [U-^{13}C]-glucose infusions in *Lm*-OVA infected mice.

(**B**) Relative contribution of infused [U-^{13}C]-glucose to the indicated metabolites in CD8$^+$ naïve (Tn; CD8$^+$CD44^{low}) T cells (*left*) and *Lm*-OVA-specific effector T (Teff) cells (*right*) at 3 days post-infection (dpi). ^{13}C metabolite enrichment is normalized relative to steady-state [U-^{13}C]-glucose (m+6) enrichment in serum (see also Figure S1A). Data represent the mean ± SEM (n = 4 mice/group).

(**C**) Schematic of major glucose-fueled metabolic pathways downstream of glucose-6-phosphate (Glc-6-P). The reaction for UGP2-dependent UDP-Glc biosynthesis is indicated.

(**D**) Timecourse of [U-^{13}C]-glucose incorporation into the metabolic pathways outlined in (C). CD8$^+$ OT-I Teff cells isolated from *Lm*-OVA-infected mice at 3 dpi were cultured *ex vivo* for up to 2 h in VIM medium containing 5 mM [U-^{13}C]-glucose. Total ^{13}C enrichment (% of pool) from [U-^{13}C]-glucose in UTP, UDP-Glc, serine, and UDP-GlcNAc is shown. Data represent the mean ± SEM (n = 3 biological replicates).

(**E**) Relative UDP-Glc abundance in Tn and OT-I Teff cells isolated from *Lm*-OVA-infected mice at 3 dpi. Data represent the mean ± SEM (n = 4 mice/group). AU, arbitrary unit.

(**F**) Schematic depicting the contribution of glucose carbon to UDP-Glc synthesis.

(**G**) Mass isotopologue distribution of [U-^{13}C]-glucose-derived UDP-Glc in CD8$^+$ Teff cells over time. CD8$^+$ OT-I Teff cells from *Lm*-OVA-infected mice as in (D) were cultured *ex vivo* for up to 2 h in VIM medium containing 5 mM [U-^{13}C]-glucose. Data represent the mean ± SEM (n = 3 biological replicates).

(**H**) Mass isotopologue distribution of [U-^{13}C]-glucose-derived UDP-Glc in mouse and human CD8$^+$ T cells. *In vitro*-activated CD8$^+$ T cells were cultured for 2 h in VIM medium containing 5 mM [U-^{13}C]-glucose prior to metabolite extraction. Data represent the mean ± SEM (n = 4 mice and 3 human donors).

Figure 2: UGP2 coordinates UDP-Glc biosynthesis in T cells to maintain T cell homeostasis and fuel CD8$^+$ Teff cell responses to infection.

(**A**) Targeting strategy for T cell-specific deletion of *Ugp2* in mice (*Ugp2*$^{fl/fl}$*Cd4-Cre* strain).

(**B**) Representative flow cytometry plots for CD19 versus CD3 expression from splenocytes isolated from control *Ugp2*$^{fl/fl}$ (+/+) and knockout *Ugp2*$^{fl/fl}$*Cd4-Cre* (-/-) mice.

(**C**) Percentage (*left*) and total number (*right*) of CD3$^+$ T cells in the spleen of *Ugp2*$^{fl/fl}$ (+/+) and *Ugp2*$^{fl/fl}$*Cd4-Cre* (-/-) mice. Data represent the mean ± SEM (n = 6 mice/group; circle = female, square = male).

(**D**) Representative flow cytometry plots for CD8A versus CD4 expression (gated on CD3$^+$ cells) from splenocytes isolated from *Ugp2*$^{fl/fl}$ (+/+) and *Ugp2*$^{fl/fl}$*Cd4-Cre* (-/-) mice.

(**E-F**) Peripheral T cell populations in T cell-specific UGP2-deficient mice. Percentage (*left*) and total number (*right*) of CD4$^+$ T cells (E) and CD8$^+$ T cells (F) in the spleen of control *Ugp2*$^{fl/fl}$ (+/+) and knockout *Ugp2*$^{fl/fl}$*Cd4-Cre* (-/-) mice. Data represent the mean ± SEM (n = 6 mice/group; circle = female, square = male).

(**G**) Immunoblot of UGP2 protein expression in control shRNA (shCtrl) and sh*Ugp2*-expressing CD8$^+$ T cells. ACTIN protein expression is shown as a loading control.

(**H**) Relative abundance of UDP-Glc in shCtrl and sh*Ugp2*-expressing CD8$^+$ T cells cultured *in vitro*. Data represent the mean ± SEM (n = 3). AU, arbitrary unit.

(**I**) Relative abundance of the indicated [U-^{13}C]-glucose-derived UDP-Glc mass isotopologues in shCtrl and sh*Ugp2*-expressing CD8$^+$ T cells after 24 h of culture in VIM medium containing 5 mM [U-^{13}C]-glucose. Data represent the mean ± SEM (n = 3). AU, arbitrary unit.

(**J**) Relative cell number over time for activated shCtrl and sh*Ugp2*-expressing CD8$^+$ T cells cultured *in vitro* in IMDM containing 50 U/mL IL-2. Data represent the mean ± SEM (n = 3).

(**K-M**) Expansion of UGP2-depleted CD8$^+$ OT-I cells *in vivo* in response to *Lm*-OVA infection. (K) Experimental setup for adoptive transfer of control (shCtrl) or sh*Ugp2*-expressing Thy1.1$^+$CD8$^+$ OT-I cells followed by *Lm*-OVA infection. (**L**) Representative flow cytometry plots showing the abundance of antigen-specific (Thy1.1$^+$) control and sh*Ugp2*-expressing CD8$^+$ OT-I cells in the spleen of *Lm*-OVA-infected mice at 7 days post-infection (dpi). (**M**) Percentage (*left*) and total

number (*right*) of antigen-specific (Thy1.1$^+$) control and sh*Ugp2*-expressing CD8$^+$ OT-I cells in the spleen of *Lm*-OVA-infected mice at 7 dpi. Data represent the mean ± SEM (n = 4 mice/group). (**N-O**) Cytokine response of UGP2-depleted CD8$^+$ OT-I cells *ex vivo*. (N) Representative flow cytometry plots showing the percentage of IFN-γ-producing Thy1.1$^+$ control (shCtrl) and sh*Ugp2*-expressing CD8$^+$ OT-I cells in the spleen of *Lm*-OVA-infected mice at 7 dpi after *ex vivo* re-stimulation with OVA peptide. (**O**) Percentage (*left*) and total number (*right*) of IFN-γ-producing Thy1.1$^+$ control and sh*Ugp2*-expressing CD8$^+$ OT-I cells in the spleen of *Lm*-OVA-infected mice at 7 dpi after *ex vivo* re-stimulation with OVA peptide. Data represent the mean ± SEM (n = 4 mice/group).

Figure 3: UDP-Glc fuels glycogen biosynthesis and UDP-Gal-dependent metabolic processes in CD8$^+$ T cells.

(**A**) Schematic showing metabolic pathways fueled by UDP-Glc. Metabolic intermediates are shown in black and enzymes are shown in blue.

(**B**) Total glycogen abundance in *in vitro*-activated shCtrl- (control) and sh*Ugp2*-expressing CD8$^+$ T cells. Data represent the mean ± SEM (n = 3).

(**C**) Relative abundance of UDP-Gal (*left*) and UDP-GlcA (*right*) levels in *in vitro*-activated control and sh*Ugp2*-expressing CD8$^+$ T cells. Data represent the mean ± SEM (n = 3). AU, arbitrary unit.

(**D**) N-glycan expression on the surface of activated control and sh*Ugp2*-expressing CD8$^+$ T cells. Representative histogram (*left*) and quantification of geometric mean fluorescence intensity (MFI; *right*) of ConA on control and sh*Ugp2*-expressing CD8$^+$ T cells. Data represent the mean ± SEM (n = 3).

(**E**) Glycan profiling of *in vitro*-activated control and sh*Ugp2*-expressing CD8$^+$ T cells via lectin binding. *Left*, Schematic of N-glycan extension. Sugar structures are highlighted in the legend (GlcNAc, N-acetylglucosamine; Gal, galactose; Fuc, fucose; Man, mannose; Sia, sialic acid). *Right*, geometric MFI of the indicated glycan features on the surface of CD8$^+$ T cells and the lectins that bind them. Data are plotted as the $\log_2$ fold change ($\log_2$FC) of sh*Ugp2*/shCtrl. Data represent the mean ± SEM (n = 3).

(**F**) Volcano plot of lipid levels in *in vitro*-activated control and sh*Ugp2*-expressing CD8$^+$ T cells. Specific lipid species are indicated (GA1, gangliosides; HexCer, hexosylceramides; Cer, ceramides; SM, sphingomyelins). Data are plotted as the $\log_2$ fold change ($\log_2$FC) of sh*Ugp2*/shCtrl and represent the average of 3 biological replicates. The horizontal line indicates the false discovery rate (FDR)-adjusted p value cutoff of 0.05 and the vertical line indicates a $\log_2$FC of 0.

(**G**) Relative abundance of the indicated GSLs in *in vitro*-activated sh*Ugp2*-expressing CD8$^+$ T cells relative to the mean abundance in shCtrl-expressing cells. Data represent the mean ± SEM (n = 3). Statistical significance was determined using multiple t-tests and an FDR correction for multiple comparisons. ‡, $q < 0.01$.

Figure 4: CD8$^+$ T cells direct glucose to fuel GSL biosynthesis *in vivo*.

(**A**) Protein levels of GSL biosynthesis pathway and galactosyltransferase enzymes in activated CD8$^+$ T cells *in vivo*. Data are expressed as the $\log_2$ fold change ($\log_2$FC) in protein levels in antigen-specific CD8$^+$ OT-I T effector (Teff) cells relative to CD8$^+$ naïve T (Tn) cells isolated from *Lm*-OVA-infected mice at 3 days post-infection (dpi). Data represent the mean ± SEM (n = 4-5 mice/group). Data were mined from Ma *et al.*[9].

(**B**) Relative contribution of [U-^{13}C]-glucose to the indicated GSL species (m+6) in CD8$^+$ naïve (Tn; CD8$^+$CD44^{low}) T cells and *Lm*-OVA-specific Teff cells following [U-^{13}C]-glucose infusion at 3 dpi. Mice were infused with [U-^{13}C]-glucose *in vivo* at 3 dpi as described in Figure 1A. ^{13}C metabolite enrichment is normalized relative to steady-state [U-^{13}C]-glucose (m+6) enrichment in serum (see also Figure S1A). Data represent the mean ± SEM (n = 4 mice/group). Statistical significance was determined using multiple t-tests and a false discovery rate correction for multiple comparisons. ‡, $q < 0.01$.

(**C**) Relative abundance of total (*left*) and m+6-labeled (*right*) Hex1Cer (d18:1/16:0) in Tn and Teff cells from *Lm*-OVA-infected mice infused with [U-^{13}C]-glucose *in vivo* at 3 dpi. Data represent the mean ± SEM (n = 4 mice/group). AU, arbitrary unit.

(**D**) Schematic of GA1 ganglioside biosynthesis from GlcCer.

(**E**) Relative abundance of total (*left*) and m+6-, m+12-, m+18-, and m+24-labeled (*right*) GA1 (d18:1/16:0) ganglioside in Tn and Teff cells from *Lm*-OVA-infected mice infused with [U-^{13}C]-glucose *in vivo* at 3 dpi. Data represent the mean ± SEM (n = 4 mice/group). AU, arbitrary unit.

Figure 5: Glucose-dependent GSL biosynthesis is essential for CD8⁺ T cell expansion *in vivo*.

(**A**) Schematic of the GSL biosynthesis pathway. Eliglustat inhibits GlcCer production by inhibiting the enzyme UGCG.

(**B**) Proliferation of CD8⁺ T cells as measured by VPD450 dilution after 72 h of activation *in vitro* with anti-CD3 and anti-CD28 antibodies in the presence of eliglustat (0-25 μM). Representative histograms of VPD450 staining (*left*) and quantification of the percentage of divided cells (*right*) are shown. The dashed line indicates the EC_{50} of eliglustat (4.33 μM) for inhibiting proliferation. Data represent the mean ± SEM (n = 3).

(**C**) Relative abundance of Hex1Cer (d18:1/16:0) (*left*) and GA1 (d18:1/16:0) ganglioside (*right*) in CD8⁺ T cells treated with DMSO or 4 μM eliglustat for 24 h. Data represent the mean ± SEM (n = 3). AU, arbitrary unit.

(**D**) Relative UGCG protein abundance (normalized to ACTN4 abundance) in CD8⁺ T cells as determined by LC-MS-based proteomics. Activated CD8⁺ T cells were modified using CRISPR/Cas9 gene editing with either a non-targeting control (NTC) single guide RNA (sgRNA) or a sgRNA targeting *Ugcg* (sg*Ugcg*). Data represent the mean ± SEM (n = 4).

(**E**) Relative abundance of total (*left*) and m+6-labeled (*right*) Hex1Cer (d18:1/16:0) in NTC- and sg*Ugcg*-modified CD8⁺ T cells after 24 h of culture in VIM medium containing 5 mM [U-^{13}C]-glucose. Data represent the mean ± SEM (n = 4). AU, arbitrary unit.

(**F**) Relative abundance of total (*left*) and m+6-, m+12-, m+18-, and m+24-labeled (*right*) GA1 (d18:1/16:0) ganglioside in NTC- and sg*Ugcg*-modified CD8⁺ T cells after 24 h of culture in VIM medium containing 5 mM [U-^{13}C]-glucose. Data represent the mean ± SEM (n = 4). AU, arbitrary unit.

(**G-H**) Bioenergetic profile of NTC- and sg*Ugcg*-modified CD8⁺ T cells. (G) Graphs depict the extracellular acidification rate (*left*) and oxygen consumption rate (*right*) of edited CD8⁺ T cells over time. Oligomycin (Oligo), FCCP, rotenone and antimycin A (Rot/AA), and monensin (Mon) were added to cells where indicated. (**H**) Basal ATP production rates from glycolysis, OXPHOS, and glycolysis + OXPHOS (total) in NTC- and sg*Ugcg*-modified CD8⁺ T cells. Data represent the mean ± SD (n = 10/group).

(**I**) Relative cell number over time for NTC- and sg*Ugcg*-modified $CD8^+$ T cells cultured *in vitro* in IMDM containing 50 U/mL IL-2. Data represent the mean ± SEM (n = 4). Statistical significance was determined using a two-way ANOVA.

(**J-K**) Expansion of sg*Ugcg*-modified $CD8^+$ T cells *in vivo* in response to *Lm*-OVA infection. NTC- or sg*Ugcg*-modified $Thy1.1^+CD8^+$ OT-I cells were transferred into congenic hosts, the mice were infected with *Lm*-OVA, and T cell responses in the spleen of *Lm*-OVA-infected mice were analyzed at 7 days-post infection (dpi; as in Figure 2K). (J) Representative flow cytometry plots showing the abundance of antigen-specific ($Thy1.1^+$) NTC- and sg*Ugcg*-modified $CD8^+$ OT-I cells in the spleen at 7 dpi. (**K**) Percentage (*left*) and total number (*right*) of antigen-specific ($Thy1.1^+$) NTC- and sg*Ugcg*-modified $Thy1.1^+CD8^+$ OT-I cells from (J). Data represent the mean ± SEM (n = 5-6 mice/group).

Figure 6: GSL biosynthesis is required to maintain lipid rafts at the plasma membrane.

(**A**) Global proteomic analysis of control (NTC) and UGCG-deficient (sg*Ugcg*) $CD8^+$ T cells. Data represent the average of 4 biological replicates. The proteins indicated in red had a second-generation p value of 0. The vertical line indicates a $\log_2$ fold change ($\log_2$FC) of 0.

(**B**) Pathway analysis indicating the top suppressed pathways in UGCG-deficient $CD8^+$ T cells from Figure 6A. NES, normalized enrichment score.

(**C-D**) Quantification of membrane lipid rafts as determined by cholera toxin B (CTxB) binding. Representative histogram (*left*) and quantification of relative geometric mean fluorescence intensity (MFI; *right*) of CTxB expression on (C) shCtrl- and sh*Ugp2*-expressing or (D) NTC- and sg*Ugcg*-modified $CD8^+$ T cells. Data represent the mean ± SEM (n = 3-4).

(**E**) Lipid raft aggregation following TCR crosslinking in NTC- and sg*Ugcg*-modified $CD8^+$ T cells. *Left*, Representative confocal images of an NTC- and sg*Ugcg*-modified cell stained with CTxB (green), streptavidin (magenta), and DAPI (blue) after incubation with anti-CD3ε antibody and crosslinking with biotin-labeled IgG. *Right*, Quantification of lipid raft (CTxB) aggregation and CD3ε intensity (normalized to cell size) in NTC- (n = 46) and *sgUgcg*-modified (n = 12) cells was conducted 30 min after crosslinking. Data represent the mean ± SD. Statistical significance was determined using Mann-Whitney tests. AU, arbitrary unit.

Figure 7: UGCG controls CD8$^+$ T cell cytotoxic function and anti-tumor immunity.

(**A-B**) Cytolytic activity of UGCG-deficient CD8$^+$ T cells. (A) Tumor cell kill curve for control (NTC) and UGCG-deficient (sg*Ugcg*) CD8$^+$ OT-I cells isolated from *Lm*-OVA-infected mice at 7 days post-infection (dpi). OT-I cells were co-cultured *ex vivo* with MC38-OVA cancer cells at the indicated effector:target (E:T) ratio and cancer cell viability measured after 24 h. The E:T ratio required to kill 50% of cancer cells (EC_{50}) and 95% confidence interval are indicated for each genotype. Data represent the mean ± SEM (n = 6). (**B**) Timecourse of cancer cell lysis for the experiment in (A) at a fixed effector:target ratio of 10:1. The rate constant (k) ± SEM is indicated for each genotype. Data represent the mean ± SEM (n = 6).

(**C**) Granzyme B (GZMB) production in NTC- and sg*Ugcg*-modified CD8$^+$ OT-I cells. OT-I cells isolated from *Lm*-OVA-infected mice at 7 dpi as in (A) were stained for intracellular GZMB expression. Representative histogram (*left*) and quantification of relative mean fluorescence intensity (MFI; *right*) of GZMB in NTC- and sg*Ugcg*-modified CD8$^+$ T cells. Data represent the mean ± SEM (n = 6).

(**D**) Timecourse of B16-OVA melanoma tumor growth in mice that received NTC- or sg*Ugcg*-modified CD8$^+$ OT-I cells. OT-I cells ($1x10^6$) were transferred into tumor-bearing mice 7 days post-implantation (n = 11 mice/group). Vehicle control-injected mice (n = 8) were included as a "no adoptive transfer" control. Statistical significance was determined using a mixed-effects model with Geisser-Greenhouse correction and Dunnett's multiple comparisons test.

(**E**) Kaplan-Meier curve of time-to-humane endpoint for tumor-bearing mice from (D). Statistical significance was determined using log-rank tests and a Bonferroni correction for multiple comparisons.

(**F**) Percentage of antigen-specific (Thy1.1$^+$) NTC- and sg*Ugcg*-modified CD8$^+$ OT-I cells in B16-OVA tumors 7 days post-adoptive transfer. Data represent the mean ± SEM (n = 9 mice/group).

(**G**) GZMB production in B16-OVA TILs from (F). Relative MFI of GZMB in Thy1.1$^+$CD8$^+$ NTC- and sg*Ugcg*-modified OT-I cells 7 days post-adoptive transfer. Data represent the mean ± SEM (n = 9 mice/group).

STAR METHODS

KEY RESOURCES TABLE

REAGENT or RESOURCE	SOURCE	IDENTIFIER
Antibodies		
Hamster monoclonal anti-mouse CD3ε (145-2C11)	Thermo Fisher Scientific	Cat# 16-0031-82; RRID: AB_468847
Hamster monoclonal anti-mouse CD28 (37.51)	Thermo Fisher Scientific	Cat# 16-0281-86; RRID: AB_468923
Rat monoclonal anti-mouse CD8α (53-6.7), BUV395	BD Biosciences	Cat# 563786; RRID: AB_2732919
Rat monoclonal anti-mouse CD8α (53-6.7), BUV737	BD Biosciences	Cat# 612759; RRID: AB_2870090
Rat monoclonal anti-mouse CD44 (IM7), BUV805	BD Biosciences	Cat# 741921; RRID: AB_2871234
Mouse monoclonal anti-mouse NK-1.1 (PK136), Brilliant Violet 605	BioLegend	Cat# 108739; RRID: AB_2562273
Rat monoclonal anti-mouse CD127 (A7R34), Brilliant Violet 785	BioLegend	Cat# 135037; RRID: AB_2565269
Rat monoclonal anti-mouse CD25 (PC61.5), Alexa Fluor 488	Thermo Fisher Scientific	Cat# 53-0251-82; RRID: AB_763472
Rat monoclonal anti-mouse CD3 (17A2), FITC	Thermo Fisher Scientific	Cat# 11-0032-82; RRID: AB_2572431
Rat monoclonal anti-mouse CD4 (RM4-5), FITC	Thermo Fisher Scientific	Cat# 11-0042-82; RRID: AB_464896
Hamster monoclonal anti-mouse KLRG1 (2F1), Alexa Fluor 532	Thermo Fisher Scientific	Cat# 58-5893-82; RRID: AB_2815282
Rat monoclonal anti-mouse CD19 (1D3), PE	BioLegend	Cat# 152408; RRID: AB_2629817

Mouse monoclonal anti-mouse CD90.1/Thy1.1 (HIS51), PE	Thermo Fisher Scientific	Cat# 12-0900-81; RRID: AB_465773
Mouse monoclonal anti-human/mouse Granzyme B (QA16A02), PE/Dazzle 594	BioLegend	Cat# 372216; RRID: AB_2728383
Rat monoclonal anti-mouse CD8α (53-6.7), PE-Cyanine7	Thermo Fisher Scientific	Cat# 25-0081-82; RRID: AB_469584
Rat monoclonal anti-mouse TNF-alpha (MP6-XT22), PE-Cyanine7	Thermo Fisher Scientific	Cat# 25-7321-82; RRID: AB_11042728
Rat monoclonal anti-mouse CD4 (RM4-5), APC	Thermo Fisher Scientific	Cat# 17-0042-82; RRID: AB_469323
Rat monoclonal anti-mouse IFN-gamma (XMG1.2), APC	Thermo Fisher Scientific	Cat# 17-7311-82; RRID: AB_469504
Rabbit polyclonal anti-UGP2	Proteintech	Cat# 10391-1-AP; RRID: AB_2272775
Rabbit polyclonal anti-β-ACTIN	Cell Signaling Technology	Cat# 4967; RRID: AB_330288
Goat anti-rabbit IgG, HRP-conjugated	Cell Signaling Technology	Cat# 7074; RRID: AB_2099233
Goat polyclonal anti-Armenian hamster IgG (H+L), secondary antibody, biotin-conjugated	Thermo Fisher Scientific	Cat# 13-4113-85; RRID: AB_466651
Bacterial and Virus Strains		
Attenuated (ΔactA) *Lm*-OVA	John Harty	Haring *et al.*[64]
Chemicals, Peptides, and Recombinant Proteins		
DMEM with 4.5 g/L glucose and L-glutamine, without sodium pyruvate	Wisent Inc.	Cat# 319-015-CL
IMDM with L-glutamine & 25 mM HEPES	Wisent Inc.	Cat# 319-105-CL

ImmunoCult-XF T Cell Expansion Medium	StemCell Technologies	Cat# 10981
Van Andel Institute-modified IMDM (VIM)	Custom	Kaymak *et al.*[15]
Seahorse XF base medium, without phenol red	Agilent Technologies	Part# 103335-100
Nu-Serum IV Culture Supplement	Corning	Cat# 355504; Lot# 2080003
Fetal bovine serum (FBS), heat-inactivated	Corning	Cat# 35-016-CV; Lot# 16821001
Fetal bovine serum (FBS), dialyzed	Corning	Cat# 35-071-CV; Lot# 35071105
Pen Strep (5,000 U/mL penicillin and 5,000 μg/mL streptomycin)	Gibco	Cat# 15070063
2-mercaptoethanol (55 mM; 1000x)	Gibco	Cat# 21985023
Recombinant murine IL-2	Peprotech	Cat# 212-12
Recombinant human IL-2	Peprotech	Cat# 200-02
ImmunoCult Human CD3/CD28 T Cell Activator	StemCell Technologies	Cat# 10971
Eliglustat	Selleck	S7852
D-Glucose [U-$^{13}C_6$]	Cambridge Isotopes	Cat# CLM-1396
D-Glucose	Sigma-Aldrich	Cat# G8270
L-Glutamine	Sigma-Aldrich	Cat# G3126
Fixable Viability Dye eFluor 506	Thermo Fisher Scientific	Cat# 65-0866-14
Fixable Viability Dye eFluor 780	Thermo Fisher Scientific	Cat# 65-0865-14
Violet Proliferation Dye 450	BD Biosciences	Cat# 562158

BD GolgiStop	BD Biosciences	Cat# 51-2092KZ
Foxp3/Transcription Factor Staining Buffer Set	Thermo Fisher Scientific	Cat# 00-5523-00
Hexadimethrine bromide (Polybrene)	Sigma-Aldrich	Cat# 107689
$OVA_{257-264}$ (SIINFEKL) peptide	AnaSpec	Cat# AS-60193-1
Lenti-X concentrator	Takara Bio	Cat# 631232
cOmplete, EDTA-free (protease inhibitor cocktail tablets)	Roche	Cat# 11873580001
PhosSTOP (phosphatase inhibitor cocktail tablets)	Roche	Cat# 4906845001
Monensin sodium salt	Sigma-Aldrich	Cat# M5273
Cholera Toxin B subunit (CTxB), FITC	Sigma-Aldrich	Cat# C1655
Phaseolus vulgaris Erythroagglutinin (PHA-E), Fluorescein	Vector Laboratories	Cat# FL-1121-2
Phaseolus vulgaris Leucoagglutinin (PHA-L), Fluorescein	Vector Laboratories	Cat# FL-1111-2
Aleuria aurantia Lectin (AAL), Fluorescein	Vector Laboratories	Cat# FL-1391-1
Galanthus nivalis Lectin (GNL), Fluorescein	Vector Laboratories	Cat# FL-1241-2
Griffonia (*Bandeiraea*) *simplicifolia* Lectin I (GSL I, BSL I), Fluorescein	Vector Laboratories	Cat# FL-1101
Griffonia (*Bandeiraea*) *simplicifolia* Lectin II (GSL II, BSL II), Fluorescein	Vector Laboratories	Cat# FL-1211-2
Datura stramonium Lectin (DSL), Fluorescein	Vector Laboratories	Cat# FL-1181-2
Streptavidin, Alexa Fluor 647	Thermo Fisher Scientific	Cat# S21374
Cas9 nuclease 2NLS, *S. pyogenes* (*Sp*-Cas9; 1000 pmol at 20 μM)	Synthego	Add-on product

Critical Commercial Assays		
EasySep Mouse T cell Isolation Kit	StemCell Technologies	Cat# 19851
EasySep Mouse $CD8^+$ T cell Isolation Kit	StemCell Technologies	Cat# 19853
EasySep Mouse Naïve $CD8^+$ T cell Isolation Kit	StemCell Technologies	Cat# 19858
EasySep Mouse CD90.1 Positive Selection Kit	StemCell Technologies	Cat# 18958
Seahorse XFe96 FluxPak	Agilent Technologies	Part# 102416-100
Seahorse XF Cell Mito Stress Test Kit	Agilent Technologies	Part# 103015-100
Lipofectamine 2000 Transfection Reagent	Thermo Fisher Scientific	Cat# 11668019
Glycogen-GLO Assay	Promega	Cat# J5051
Pierce BCA Protein Assay Kit	Thermo Fisher Scientific	Cat# 23225
Pierce Rapid Gold BCA Protein Assay Kit	Thermo Fisher Scientific	Cat# A53227
P3 Primary Cell 4D-Nucleofector X Kit S	Lonza	Cat# V4XP-3032
Deposited data		
Proteomics data	This manuscript	PRIDE: PXD056453
Experimental Models: Cell Lines		
293T cells	ATCC	CRL-3216
MC38-OVA-tdTomato cells		Luda *et al.*[16]
B16-OVA cells		Cordeiro *et al.*[65]
Experimental Models: Organisms/Strains		

C57BL/6J mice	The Jackson Laboratory	RRID: IMSR_JAX:000664
C57BL/6-Tg(TcraTcrb)1100Mjb/J (OT-I) mice	The Jackson Laboratory	RRID: IMSR_JAX:003831
B6.PL-*Thy1*^{a}/CyJ (Thy1.1) mice	The Jackson Laboratory	RRID: IMSR_JAX:000406
B6.Cg-Tg(Cd4-cre)1Cwi/BfluJ (*Cd4-Cre*) mice	The Jackson Laboratory	RRID: IMSR_JAX:022071
Ugp2-floxed mice	This paper	
Oligonucleotides		
Ugp2 exon 2-targeting sgRNAs: Upstream: AAAGAGCGTGTCCTTTATATAGG Downstream: TAATCCTGTCCATGCTCTTTTGG	This paper	Custom
Ugp2 donor template (933-nt megamer): AGTATACTCTGGAATCCCACAGGTGTAGGTTCTTAAT GGCAGTGAATGAATGAACTTAACAACAAGAGTGAAG GCAGGCAGGCAAAGAGCGTGTCCTTTAATAACTTCGT ATAATGTATGCTATACGAAGTTATTATAGGCTGCCAG TAGAAGATGTGGTGCACATTAAAGGTAGATCTTCCCA CCTCAGAGATCCAGATTACAGGTGGGTCTTCCTACTTC AAATAATCTAATTAAGCAAAATCCCTTAAAGGTGTAC CCAGCCTCTTGGGTTTTAGTTAAGCTAAATGTTGTCAA GTTGACAGCCATCACTCTTTGTTTAGCATACTTCCATC TTGTTATAAAGCAAAGGCCAACAAATTCTCAGACTTT GGTCCATCTTGACTTTAATCTGTAAATAACAAAATTAA TAAGTTTCCTTGTTGCTGACTGATACTAATCAGTGACT TTATATTTTTTTATTTAAGATCTTAGCAAAGCTATGTCT CAAGATGGTGCTTCTCAGTTCCAAGAGGTCATTCTCC AAGAACTAGAATTATCTGTGAAGAAAGAATTAGAAA AAATACTTACCACAGCAGCCTCACATGAGTTTGAGGT AAGGATTCAATAGTGTCTTTTGCTTTGTGTGTCAACAT GCATAATTGCCACCAGTGGTGATTCTCCAGCCTGAAA TGAGCACAGGATGTAACATCAGAAGTTAGCACTGTTG AACACTCACAGATCGTTAATATTTGTTCATAGTACAGC	This paper	Custom

TACTTTCTTTTGTTAAAAAAAAAAACTGAGGAAATTTT CCAAGTCCCCAAAAATAACTTCGTATAATGTATGCTAT ACGAAGTTATGAGCATGGACAGGATTACAGTTTATGT TGTGTTTGAGTATCATTGGGTATAGAGATGGTTACCA TGTTTAGTCGGATCTGTAACAAGCCATGTCCTCTCT		
Genotyping primers for upstream (5') *loxP* site: Forward: AGGTGTAGGTTCTTAATGGCAGT Reverse: CAGGCTGGAGAATCACCACT		
Genotyping primers for downstream (3') *loxP* site: Forward: CTTACCACAGCAGCCTCACAT Reverse: TTCTCACCAAAAGAACAAAAAGGGA		
Firefly luciferase shRNA (LMPd-Amt backbone): AGCTCCCGTGAATTGGAATCCTAGTGAAGCCACAGAT GTAGGATTCCAATTCAGCGGGAGCC	Matthew Pipkin	Chen *et al.*[66]
Ugp2 shRNA (LMPd-Amt backbone): GGGCTAAAGAGTTTCTTATAATTACATCTGTGGCTTCA CTAATTATAAGAAACTCTTTAGCCT	This paper	Custom
Non-targeting control (NTC) gRNA: GCACUACCAGAGCUAACUCA	Synthego	Nüssing *et al.*[67]
Ugcg-targeting sgRNA: UCCAACUCACGUGUAGAUGA	Synthego	Custom
Recombinant DNA		
pLMPd-Ametrine (LMPd-Amt)	Matthew Pipkin	Chen *et al.*[66]
pCL-Eco	Steven Reiner	Plasmid #12371 (Addgene)
Software and Algorithms		

Adobe Illustrator v28.1	Adobe	adobe.com/products/illustrator.html
Fiji v2.15.1		imagej.net/software/fiji
FlowJo v9.9.5	FlowJo LLC	flowjo.com
GraphPad Prism v9-10	GraphPad Software	graphpad.com
IncuCyte v2022A Rev1	Sartorius	sartorius.com/en
LipidSearch v5.0	Thermo Fisher Scientific	thermofisher.com
R v4.4.0		cran.r-project.org
Skyline v22-23	MacCoss Lab Software	skyline.ms
Spectronaut v18	Biognosys	biognosys.com/software/spectronaut

RESOURCE AVAILABILITY

Lead Contact

Additional information and requests for raw data or reagents should be directed to, and will be made available by, the corresponding author, Dr. Russell G. Jones (russell.jones@vai.org).

Materials availability

All unique, stable reagents generated in this study will be made available from the Lead Contact with a completed Material Transfer Agreement. The LMPd-Amt-sh*Ugp2* plasmid will be deposited to Addgene.

Data and code availability

The mass spectrometry proteomics data have been deposited to the ProteomeXchange Consortium via the PRIDE partner repository with the dataset identifier PXD056453. The

proteomics data and confocal image analysis pipelines are hosted on GitHub (see METHOD DETAILS for links).

EXPERIMENTAL MODEL AND SUBJECT DETAILS

Mice

C57BL/6J (RRID: IMSR_JAX:000664), B6.PL-*Thy1*^{a}/CyJ (Thy1.1; RRID: IMSR_JAX:000406), C57BL/6-Tg(TcraTcrb)1100Mjb/J (OT-I; RRID: IMSR_JAX:003831), and B6.Cg-Tg(Cd4-cre)1Cwi/BfluJ (*Cd4-Cre*; RRID: IMSR_JAX:022071) mice were purchased from The Jackson Laboratory. Homozygous Thy1.1 mice were crossed to homozygous OT-I mice to generate heterozygous Thy1.1 OT-I mice, which were used to isolate Thy1.1$^+$CD8$^+$ OT-I cells. All mice were bred and maintained in grouped housing at the Van Andel Institute (VAI) Vivarium under specific pathogen-free conditions. All procedures involving mice were completed as recommended in the Guide for the Care and Use of Laboratory Animals, and all protocols were approved by VAI's Institutional Animal Care and Use Committee (IACUC). Genotyping was performed using DNA extracted from ear biopsies and defined primer sets[16] (see **Key Resource Table**). Experiments were performed using female mice between 8-12 weeks of age, unless otherwise indicated.

Cell lines

293T cells (CRL-3216), MC38 murine colon cancer cells expressing OVA and tdTomato (MC38-OVA-tdTomato)[16], and B16-F10 murine melanoma cells expressing OVA (B16-OVA)[65] were cultured in Dulbecco's Modified Eagle's Medium (DMEM) (Wisent Inc.) supplemented with 10% heat-inactivated fetal bovine serum (FBS), 1% penicillin-streptomycin (Gibco; [final] = 50 U/mL penicillin and 50 μg/mL streptomycin), and L-glutamine at a final concentration of 6 mM. 293T and MC38-OVA-tdTomato cells are female, and B16-OVA cells are male. All cells were cultured at 37°C in a humidified 5% CO_2 incubator.

Primary cells

Frozen human peripheral blood CD8$^+$ T cells from three different healthy donors were purchased from StemCell Technologies (Cat# 200-0164). Two donors were female (Lot# 2210425008 and

2210427003) and one donor was male (Lot# 2210403009). Cells were cultured in ImmunoCult-XF T Cell expansion Medium (StemCell Technologies) supplemented with 50 U/mL penicillin and 50 μg/mL streptomycin (Gibco) and 300 U/mL recombinant human IL-2 (Peprotech) at 37°C in a humidified 5% CO_2 incubator. Cells were activated for 72 h with ImmunoCult Human CD3/CD28 T Cell Activator (StemCell Technologies; 25 μL per $1x10^6$ cells in 1 mL final volume).

METHOD DETAILS

Generation of Ugp2-floxed mice

Ugp2-floxed animals were generated by CRISPR/Cas9 gene editing at the McGill Integrated Core for Animal Modeling, as previously described[68]. Single gRNA (sgRNA) sequences flanking *Ugp2* exon 2 were purchased from Synthego and the single-stranded megamer (933-nt) donor template was purchased from Integrated DNA Technologies (IDT; see **Key Resources Table**). The sgRNAs (25 ng/μL each) were complexed with Alt-R *Sp*-Cas9 Nuclease V3 (IDT, Cat# 1081059; 50 ng/μL) and microinjected simultaneously with the donor template (20 ng/μL) into the pronucleus of zygotes from C57BL/6J mice. After microinjection, the embryos were implanted into pseudo-pregnant CD-1 female mice for gestation, as described previously[68]. Successful *loxP* insertion was confirmed using PCR primers flanking the mutation sites (see **Key Resources Table**) followed by Sanger sequencing. *Ugp2*-floxed mice were crossed to hemizygous *Cd4-Cre* mice to generate $Ugp2^{fl/fl}$*Cd4-Cre* mice. Cre-negative $Ugp2^{fl/fl}$ mice were used as controls.

T cell purification and culture

For mouse T cell isolations, total ($CD3^+$) T cells, total $CD8^+$ T cells, or naïve $CD8^+$ T cells were purified from the spleen and peripheral lymph nodes by negative selection (StemCell Technologies). Cells were cultured in Iscove's Modified Dulbecco's Medium (IMDM; Wisent Inc.) supplemented with 10% Nu-Serum IV culture supplement (Corning), 50 U/mL penicillin and 50 μg/mL streptomycin (Gibco), 50 μM 2-mercaptoethanol (Gibco), and 2 mL L-glutamine (Gibco; 6 mM final concentration). T cells ($1x10^6$ cells/mL) were activated *in vitro* via stimulation with plate-bound anti-CD3ε (clone 145-2C11; 2 μg/mL) and anti-CD28 (clone 37.51; 1 μg/mL) antibodies for 48-72 hr. After activation, cells were propagated in IMDM supplemented with 50 U/mL

recombinant murine IL-2 (Peprotech). Proliferating cells were re-seeded at $4x10^5$ cells/mL in fresh medium and IL-2 every two days.

shRNA cloning, retrovirus production, and viral transduction

Short hairpin RNAs (shRNAs) against firefly luciferase (shCtrl) or *Ugp2* (sh*Ugp2*; see **Key Resources Table** for sequences) were subcloned into the pLMPd-Amt vector between the XhoI and EcoRI restriction enzyme sites[66]. 293T cell transfection, retrovirus production, and viral transduction of activated $CD8^+$ T cells were performed as previously described[16].

CRISPR/Cas9 gene editing in primary $CD8^+$ T cells

A singe guide RNA (sgRNA) targeting the murine *Ugcg* gene (5'–UCCAACUCACGUGUAGAUGA–3') and a non-targeting control (NTC) sgRNA (5'–GCACUACCAGAGCUAACUCA–3')[67] were obtained from Synthego (CRISPRevolution sgRNA EZ Kit). For sgRNA/Cas9 ribonucleoprotein (RNP) complex formation, 1.86 μL of *Sp*-Cas9 nuclease (Synthego) was combined with 3.4 μL of target sgRNA (0.1 nmol/μL stock in nuclease-free water) and incubated for 10 min at room temperature. In the meantime, $2.5x10^6$ activated $CD8^+$ T cells were pelleted, washed twice with phosphate-buffered saline (PBS), and resuspended in 20 μL of P3 solution mix (P3 Primary Cell 4D-Nucleofector X Kit S, Lonza). After RNP complex formation, the cells were added to the RNP complex mixture, and the RNP/cell mixture was then transferred to a well of a 16-well Nucleocuvette Strip (Lonza). Cells were electroporated using a 4D-Nucleofector (Lonza; program DN 100). Immediately after electroporation, 150 μL of 37°C pre-warmed IMDM (antibiotic-free) was added to the cells, which were then left to rest at 37°C for 10 min. Cells were transferred to 2.5 mL of IMDM (antibiotic-free) in a well of a 12-well plate. The cells were used for adoptive transfer or other experiments 2-3 days post-electroporation. Knockout of *Ugcg* was confirmed by LC-MS and/or CTxB staining.

Adoptive transfer and infection with L. monocytogenes (Lm-OVA)

Mice were immunized intravenously with a sublethal dose of recombinant attenuated *Listeria monocytogenes* expressing OVA (*Lm*-OVA; $2x10^6$ colony-forming units (CFU)), as previously described[16,69]. For adoptive transfer experiments involving immunophenotyping at 7 days post-

infection (dpi), $5x10^3$ Thy1.1$^+$CD8$^+$ OT-I cells were injected intravenously into Thy1.2$^+$ C57BL/6J mice, followed by *Lm*-OVA infection 1 day later. Splenocytes were isolated from mice at 7 dpi and analyzed *ex vivo* by flow cytometry. For *in vivo* ^{13}C-glucose infusion or *ex vivo* ^{13}C-glucose tracing experiments, Thy1.2$^+$ C57BL/6J mice received $2x10^6$ Thy1.1$^+$CD8$^+$ OT-I cells intravenously and were infected with *Lm*-OVA 1 day later. Naïve CD8$^+$ or *Lm*-OVA-activated (Thy1.1$^+$) OT-I cells were isolated from the spleen of infected mice at 3 dpi using an EasySep mouse CD90.1 (Thy1.1) positive selection kit (StemCell Technologies), as previously described[9,19]. For the *ex vivo* T cell killing assay, $1\text{-}5x10^5$ Thy1.1$^+$CD8$^+$ OT-I cells were transferred into Thy1.2$^+$ C57BL/6J mice, followed by *Lm*-OVA infection 1 day later. At 7 dpi, *Lm*-OVA-activated (Thy1.1$^+$) OT-I cells were isolated from the spleen of infected mice using an EasySep mouse CD90.1 (Thy1.1) positive selection kit (StemCell Technologies).

Flow cytometry

Single-cell suspensions were prepared by mechanical dissociation of harvested lymphoid tissues followed by red blood cell lysis, as previously described[9,19]. Single-cell suspensions (cultured cells or dissociated lymphoid tissues) were stained with a cocktail of fluorescently-labeled antibodies, lectins, and/or dyes listed in the **Key Resources Table**. Cell viability was assessed by using Fixable Viability Dye (FVD) eFluor 506 or FVD eFluor 780 according to the manufacturer's protocols. Cell proliferation was assessed by Violet Proliferation Dye 450 (VPD450) dilution according to the manufacturer's protocol. To assess cytokine production, splenocytes were isolated from *Lm*-OVA-infected mice at 7 dpi and stimulated with 1 μg/mL of $OVA_{257\text{-}264}$ peptide and 50 U/mL IL-2 for 4 h, with GolgiStop (1:1500 dilution) added for the last 2 h of stimulation. After stimulation, cells were stained with surface marker antibodies in staining buffer (PBS with 2% FBS and 0.02% sodium azide) at 4°C for 1 h, fixed and permeabilized at 4°C for 1 h using the Foxp3/Transcription Factor Staining Buffer Set, and then stained with intracellular marker antibodies for either 1 h or overnight at 4°C. For cytokine profiling of Ametrine$^+$ cells, cells were briefly fixed with 4% paraformaldehyde at room temperature for 5 min prior to fixation and permeabilization with the Foxp3/Transcription Factor Staining Buffer Set. For lectin staining, cells were stained with 2 μg/mL of each lectin individually at a density of $1x10^6$ cells/mL in staining buffer for 45 min at 4°C.

Analytical flow cytometry was performed on a Cytek Aurora or BD Accuri C6 Plus cytometer. Cell sorting was performed on an Astrios or BD FACSAria Fusion cytometer. Data analysis was performed using FlowJo (v9.9.5) software.

Extracellular flux analysis

T cell oxygen consumption rate (OCR) and extracellular acidification rate (ECAR) were measured by a Seahorse XF96 Extracellular Flux Analyzer as previously described[16]. Briefly, activated NTC- or sg*Ugcg*-modified CD8$^+$ T cells (1x10^5/well) were seeded in Seahorse XF medium containing 5 mM glucose, 0.5 mM glutamine, and 1 mM sodium pyruvate and centrifuged in a poly-D-lysine-coated XF96 plate. Cellular bioenergetics was assessed at regular time intervals following the sequential addition of oligomycin (2 μM), carbonyl cyanide 4-(trifluoromethoxy)phenylhydrazone (FCCP; 1.5 μM), rotenone/antimycin A (0.5 μM each), and monensin (20 μM). Data were normalized to cell number. Bioenergetics data analysis was based on protocols developed by Mookerjee et al.[70], as previously described[16].

Stable isotope labeling

Stable isotope labeling experiments in *in vitro*-activated T cells using liquid chromatography coupled to mass spectrometry (LC-MS) were conducted as previously described[15]. Briefly, CD8$^+$ T cells were activated as above, washed with VIM medium, and re-seeded (e.g., 2 x 10^6 cells/well in a 24-well plate for up to 2 h, or 2-3 x 10^6 cells/well in a 6-well plate for 24 h) for the indicated times in VIM medium containing 10% dFBS, 50 μM 2-mercaptoethanol, and 5 mM [U-^{13}C]-glucose. Mouse T cells were further supplemented with 50 U/mL of recombinant murine IL-2 and human T cells with 300 U/mL of recombinant human IL-2. Cells were transferred from tissue culture plates to tubes and centrifuged at 600 RCF for 2 min at 4°C. The cell pellet was washed with ice-cold saline before being snap-frozen on dry ice and stored at -80°C. For *ex vivo* stable isotope labeling experiments, Thy1.1$^+$ OT-I cells were isolated from the spleen of *Lm*-OVA-infected mice at 3 dpi by magnetic bead sorting as previously described[9,19], washed with VIM medium, and re-seeded at 2 x 10^6 cells/well in a 24-well plate for the indicated times in VIM medium

containing 10% dFBS, 50 μM 2-mercaptoethanol, 5 mM [U-^{13}C]-glucose, and 50 U/mL of recombinant murine IL-2.

Stable isotope in vivo infusions

[U-^{13}C]-glucose *in vivo* infusions of *Lm*-OVA-infected mice at 3 dpi were conducted as previously described[9,16,19]. Briefly, mice were fasted for 4 h prior to infusion. Mice were anesthetized using isoflurane and infused intravenously with 100 mg/mL [U-^{13}C]-glucose (dissolved in sterile saline) over a 2 h period. An initial [U-^{13}C]-glucose bolus of 0.6 mg/g mouse was administered, followed by a 2 h [U-^{13}C]-glucose infusion at a rate of 0.125 μL/min/g mouse. Mice were euthanized via cervical dislocation and blood was harvested via cardiac puncture. Blood was centrifuged at 17,000 RCF for 10 min at 4°C to isolate serum, which was snap-frozen on dry ice and stored at -80°C. Spleens were harvested and processed for naïve CD8$^+$ or Thy1.1$^+$ T cell isolation as previously described[9,19]. Isolated T cells were snap-frozen on dry ice and stored at -80°C. T cells and serum were processed for metabolomics and lipidomics analyses as described below.

Metabolite and lipid extraction for LC-MS

Several extraction approaches were used depending on specific experimental goals. For experiments requiring both metabolite and lipid quantification, a Bligh-Dyer extraction[71] (2:2:1.8 v/v chloroform:methanol:water) was used. Samples were homogenized in a 1:1 mixture of ice-cold chloroform (Sigma, 1024441000) and methanol (Fisher Scientific, A456). After solvent addition, extracts were vortexed for 10 s, sonicated for 5 min, and incubated on wet ice for 30 min. Incubation was followed by the addition of 0.9 volumes of LC-MS-grade water (Fisher Scientific, W6) to achieve the final 2:2:1.8 ratio. For serum samples, water content of the sample was accounted for (reported as 92%) to precisely maintain the 2:2:1.8 ratio when performing the water addition. Samples were then vortexed for an additional 10 s and followed with incubation on wet ice for 10 min.

For experiments requiring only metabolomics, a single phase AMW20 (40% acetonitrile, 40% methanol, and 20% water) extraction was used. For experiments requiring only lipidomics, a HEX:IPA (50% hexane and 50% isopropanol) extraction was used. For both AMW20 and HEX:IPA

extracts, samples were homogenized with either ice-cold 4:4:2 acetonitrile:methanol:water or 1:1 hexane:isopropanol, respectively. After solvent addition, extracts were vortexed for 10 s, sonicated for 5 min, and incubated on wet ice for 1 h. Following the final incubation steps, Bligh-Dyer, AMW20, and HEX:IPA samples were centrifuged at 17,000 RCF for 10 min at 4°C. 32 µL serum equivalents of aqueous phase supernatant and 11.6 µL serum equivalents of organic phase subnatant were collected for metabolomics and lipidomics, respectively, and dried in a vacuum evaporator. In all extraction types, the extraction solvent:sample ratio was controlled within each experiment to avoid influence of varying extraction efficiency. However, for *in vivo* [U-^{13}C]-glucose infusion experiments, T cells were extracted in a fixed 1 mL volume of chloroform:methanol:water (2:2:1.8), and protein content of the insoluble fraction was used to correct detected peak areas to starting cell amount.

Aqueous metabolomics samples were resuspended in LC-MS-grade water, and organic lipidomics samples were resuspended in a 1:1 mixture of LC-MS-grade isopropanol (Fisher Scientific, A461) and acetonitrile (Fisher Scientific, A955). 640 nL serum equivalents were injected on column for metabolomics, and 116 nL serum equivalents were injected on column for lipidomics. Injected on-column cell equivalents varied per experiment based on cell availability and ranged from 48,855-276,800 cell equivalents for metabolomics and 96,000-276,800 cell equivalents for lipidomics.

Metabolomics analysis

Metabolomic profiling and stable isotope tracing data were collected using a Vanquish LC system coupled to an Orbitrap Exploris 240 (Thermo Fisher Scientific) using a heated electrospray ionization (H-ESI) source in negative mode, as previously described[16,72]. 2 µL of each standard and/or sample was injected and run through a 24-min reversed-phase chromatography Zorbax RRHD extend-C18 Column (1.8 µm, 2.1 mm x 150 mm; Agilent, 759700-902) combined with a Zorbax extend-C18 guard column (1.8 µm, 2.1 mm x 5 mm; Agilent, 821725-907). Mobile phase A consisted of LC-MS-grade water with 3% LC-MS-grade methanol, mobile phase B was LC-MS-grade methanol and both mobile phases contained 10 mM tributylamine (Sigma, 90780), 15 mM LC-MS-grade acetic acid (Fisher Scientific, A11350), and 0.01% medronic acid (v/v; Agilent, 5191-

4506). For the wash gradient, mobile phase A was kept the same, and mobile phase B was 99% LC-MS-grade acetonitrile. Column temperature was kept at 35°C, flow rate was held at 0.25 mL/min, and the chromatography gradient was as follows: 0-2.5 min held at 0% B, 2.5-7.5 min from 0% B to 20% B, 7.5-13 min from 20% B to 45% B, 13-20 min from 45% B to 99% B, and 20-24 min held at 99% B. A 16-min wash gradient was run in reverse flow direction between every injection to back-flush the column and to re-equilibrate solvent conditions as follows: 0-3 min held at 100% B and 0.25 mL/min, 3-3.5 min held at 100% B and ramp to 0.8 mL/min. 3.5-7.35 min held at 100% B and 0.8 mL/min, 7.35-7.5 min held at 100% B and ramp to 0.6 mL/min, 7.5-8.25 min from 100% B to 0% B and ramp to 0.4 mL/min, 8.25-15.5 min held at 0% B and ramp to 0.25 mL/min, and 15.5-16 min held at 0% B and 0.25 mL/min. Mass spectrometer parameters were: source voltage -2500 V, sheath gas 60, aux gas 19, sweep gas 1, ion transfer tube temperature 320°C, and vaporizer temperature 250°C. Full scan data were collected using the Orbitrap with a scan range of 70-850 m/z at a resolution of 240,000 and RF lens at 35%. Fragmentation was induced in the Orbitrap using assisted higher-energy collisional dissociation (HCD) collision energies at 15, 30, and 45%. Orbitrap resolution was 15,000, the isolation window was 2 m/z, and data-dependent scans were capped at 5 scans. Targeted mass, data-dependent MS2 (ddMS2) triggers were included for a panel of compounds (**Table S3**).

To chromatographically resolve UDP-Glc and UDP-Gal, we utilized a BEH amide chromatography with high-pH mobile phases on a Thermo Vanquish Horizon LC system coupled to an Orbitrap ID-X (Thermo Fisher Scientific) using an H-ESI source in negative mode. 2 μL of each standard and/or sample was injected on column. The 20-min chromatography used an Acquity UPLC BEH Amide Column (1.7 μm, 2.1 mm x 150 mm; Waters, 176001909) combined with an Acquity UPLC BEH Amide VanGuard Pre-column (1.7 μm, 2.1 mm x 5 mm; Waters, 186004799). Buffer A consisted of 100% LC-MS-grade water, 0.1% ammonium hydroxide (Fisher Scientific, A470), 0.1% medronic acid, 10 mM ammonium acetate (Sigma, 73594), and buffer B consisted of 90% LC-MS-grade acetonitrile, 10% LC-MS-grade water, 0.1% ammonium hydroxide, 0.1% medronic acid, and 10 mM ammonium acetate. Column temperature was kept at 40°C, flow rate was held at 0.4 mL/min, and the chromatography gradient was as follows: 0-1 min from 100% B to 90% B, 1-12.5 min from 90% B to 75% B, 12.5-19 min from 75% B to 60% B, and 19-20 min held

at 60% B. A 30-min wash gradient was run between every injection to flush the column and to re-equilibrate solvent conditions as follows: 0-1 min held at 65% B and 0.4 mL/min, 1-13 min held at 65% B and ramp to 0.8 mL/min, 13-24 min held at 65% B and 0.8 mL/min, 24-24.5 min from 65% B to 100% B and held at 0.8 mL/min, 24.5-26 min held at 100% B and ramp to 1.2 mL/min, 26-28 min held at 100% B and 1.2 mL/min, 28-29 min held at 100% B and ramp to 0.4 mL/min, and 29-30 min held at 100% B and 0.4 mL/min. For Chromatography 1, the mass spectrometer parameters were: source voltage -2500 V, sheath gas 60, aux gas 19, sweep gas 1, ion transfer tube temperature 300°C, and vaporizer temperature 250°C. Full scan data were collected using the Orbitrap with a scan range of 70-1000 m/z at a resolution of 120,000 and RF lens at 35%. In tandem with the full scan, a targeted single ion scan (tSIM) was performed in the Orbitrap to target UDP-Glc and UDP-Gal and all their ^{13}C isotopologues with a center mass of 565.0477 m/z and an isolation window 32 m/z. Resolution was set at 60,000, RF lens at 60%, and scan time was set for 10.5-13.5 min of the chromatographic gradient described above. ddMS2 fragmentation was induced in the Orbitrap using assisted HCD collision energies at 20, 40, 60, 80, 100% as well as with collision-induced dissociation (CID) at a collision energy of 35%. For both MS2 fragmentations, Orbitrap resolution was 30,000, the isolation window was 1.5 m/z, and total cycle time was 0.6 s. A targeted mass MS2 trigger for UDP-Hex (565.0477 m/z) was included.

Peak picking and integration were conducted in Skyline (v22-23) using in-house curated compound lists of accurate mass MS1 and retention time of chemical standards[72]. For tracing studies, this list was expanded to include all possible ^{13}C isotopologues and natural abundance correction was completed using IsoCorrectR[73].

Lipidomics analysis

Lipidomics analysis was completed with a Thermo Vanquish Horizon LC system coupled to an Orbitrap ID-X (Thermo Fisher Scientific) using an H-ESI source in positive mode[74]. Lipids were separated with a 30-min reversed-phase chromatography Accucore C30 column (2.6 μm, 2.1 mm x 150 mm; Thermo Fisher Scientific, 27826-152130) combined with an Accucore C30 guard column (2.6 μm, 2.1 mm x 10 mm; Thermo Fisher Scientific; 27826-012105). Buffer A consisted of 60% LC-MS-grade acetonitrile, 40% LC-MS-grade water, 0.1% LC-MS-grade formic acid (Fisher

Scientific, A117), and 10 mM ammonium formate (Fisher Scientific, 70221), and buffer B consisted of 90% LC-MS-grade isopropanol, 8% LC-MS-grade acetonitrile, 2% LC-MS-grade water, 0.1% LC-MS-grade formic acid, and 10 mM ammonium formate. Column temperature was kept at 50°C, flow rate was held at 0.4 mL/min, and the chromatography gradient was as follows: 0-1 min held at 25% B, 1-3 min from 25% B to 40% B, 3-19 min from 40% B to 75% B, 19-20.5 min 75% B to 90% B, 20.5-28 min from 90% B to 95% B, 28-28.1 min from 95% B to 100% B, and 28.1-30 min held at 100% B. A 20-min wash gradient was run between every injection to flush the column and to re-equilibrate solvent conditions as follows: 0-10 min held at 100% B, 10-14 min from 100% B to 25% B, and 14-20 min held at 25% B. The mass spectrometer parameters were: source voltage 3250 V, sheath gas 40, aux gas 10, sweep gas 1, ion transfer tube temperature 300°C, and vaporizer temperature 275°C. Full scan data were collected using the Orbitrap with a scan range of 200-1700 m/z at a resolution of 500,000 and RF lens at 45%. ddMS2 fragmentation was induced in the Orbitrap using assisted HCD collision energies at 15, 30, 45, 75, 110% as well as with CID at a collision energy of 35%. For both MS2 fragmentations, Orbitrap resolution was 15,000 and the isolation window was 1.5 m/z. A m/z 184 mass trigger, indicative of phosphatidylcholines, was used for CID fragmentation. Data-dependent MS3 fragmentation was induced in the ion trap with scan rate set at “Rapid” using CID at a collision energy of 35%. MS3 scans were triggered by specific acyl chain losses for detailed analysis of mono-, di-, and triacylglycerides. Total cycle time was 2 s. Lipid identifications were assigned using LipidSearch (v5.0; Thermo Fisher Scientific), which was used to generate a compound list, and lipid peak areas were quantified in Skyline as described above.

Glycogen quantification

Cells were cultured in VIM medium containing 10% dFBS and 50 U/mL IL-2 for 24 h. $1x10^6$ cells were processed for glycogen quantification using a Glycogen-GLO Assay Kit (Promega) as per the manufacturer’s instructions. Luminescence was quantified 60 min after the addition of the glucose detection reagent using a BioTek Synergy Neo2 multi-mode plate reader. Glycogen abundance was normalized to protein content, which was measured using a Pierce Rapid Gold BCA Protein Assay Kit (Thermo Fisher Scientific).

Immunoblotting

Cells were lysed in RIPA buffer supplemented with protease and phosphatase inhibitor cocktails (Roche) on ice for ≥30 min. A Pierce BCA Protein Assay Kit (Thermo Fisher Scientific) was used to quantify protein from whole cell lysates. Equal amounts of protein were diluted in Laemmli sample buffer, boiled for 5 min, and resolved by SDS-PAGE on a 10% gel. Proteins were transferred onto nitrocellulose membranes. Membranes were blocked for 1 h in 5% non-fat milk in TBST at room temperature and incubated with primary antibodies against UGP2 or β-ACTIN (both 1:1000-diluted in 5% non-fat milk) overnight at 4°C. Membranes were washed three times for 5 min with 1x TBST, and then incubated for 1 h at room temperature with an HRP-conjugated secondary antibody diluted 1:2000 in 5% non-fat milk/TBST. Membranes were washed three times with 1x TBST and then developed using Enhanced Chemiluminescence (ECL) Western Blotting Detection Reagent (Cytivia). Antibodies are listed in the **Key Resources Table**.

Proteomics sample preparation and analysis

$5x10^6$ control and UGCG-deficient $CD8^+$ T cells were washed twice with ice-cold PBS and cell pellets were snap-frozen on dry ice. Cell lysates were extracted and digested using EasyPrep MS Sample Prep Kits (Thermo Fisher Scientific) according to the manufacturer's instructions. Dried samples were resuspended in 0.1% trifluoroacetic acid.

For global proteome quantitation analysis, data-independent acquisition (DIA) analyses were performed on an Orbitrap Eclipse mass spectrometer coupled with the Vanquish Neo LC system (Thermo Fisher Scientific). The FAIMS Pro source was positioned between the nanoESI source and the mass spectrometer. A total of 2 μg of digested peptides were separated on a nano capillary column (20 cm x 75 μm I.D., 365 μm O.D., 1.7 μm C18; CoAnn Technologies) at a flow rate of 300 nL/min. Mobile phase A was water with 0.1% formic acid, and mobile phase B was 20% water and 80% acetonitrile with 0.1% formic acid. The LC gradient was programmed as follows: 1% B to 24% B over 110 min, 85% B over 5 min, and 98% B over 5 min, resulting in a total gradient length of 120 min. For FAIMS, selected compensation voltages (-40V, -55V, -70V) were applied throughout the LC-MS/MS runs. Full MS spectra were collected at a resolution of 120,000

(FWHM), and MS2 spectra at 30,000 (FWHM). Standard automatic gain control (AGC) targets and automatic maximum injection times were used. A precursor range of 380-980 m/z was set for MS2 scans, with a 50 m/z isolation window and a 1 m/z overlap for each scan cycle. A 32% HCD collision energy was used for MS2 fragmentation.

To generate a hybrid library for directDIA analysis in Spectronaut, pooled samples underwent data-dependent acquisition (DDA) employing 11 distinct FAIMS CV settings ranging from -30 to 80 CV. Full MS spectra were collected at 120,000 resolution (FWHM), and MS2 spectra at 30,000 resolutions (FWHM). The standard AGC target and automatic maximum injection time were selected. Ions with charges of 2-5 were filtered. An isolation window of 1.6 m/z was used with quadrupole isolation mode, and ions were fragmented using HCD with a collision energy of 32%.

For the targeted quantitation, parallel reaction monitoring (PRM) was performed on an Exploris 480 mass spectrometer coupled with the Vanquish Neo LC system (Thermo Fisher Scientific). A total of 2 μg of digested peptides were separated on a nano capillary column (20 cm x 75 μm I.D., 365 μm O.D., 1.7 μm C18; CoAnn Technologies) at a flow rate of 300 nL/min. Mobile phase A was water with 0.1% formic acid, and mobile phase B was 20% water and 80% acetonitrile with 0.1% formic acid. The LC gradient was as follows: 1% B to 26% B over 51 min, 85% B over 5 min, and 98% B over 4 min, with a total gradient length of 60 min. Full MS spectra (m/z 375-1200) were collected at a resolution of 120,000 (FWHM), and MS2 spectra at 30,000 (FWHM). Standard AGC targets and automatic maximum injection times were used for both full and MS2 scans. A 32% HCD collision energy was used for MS2 fragmentation. All samples were analyzed using a multiplexed PRM method with a scheduled inclusion list containing the target precursor ions. Three unique peptides of UGCG (QGFAATLEQVYFGTSHPR, VGLVHGLPYVADR, and SYISANVTGFK) were used to measure the relative abundance of UGCG, while two α-ACTININ 4 (ACTN4) peptides (DDPVTNLNNAFEVAEK and LVSIGAEEIVDGNAK) served as internal standards. Synthetic peptides were obtained from Biosynth.

DIA data were processed in Spectronaut v18 (Biognosys) using directDIA analysis. Data were searched against the *Mus musculus* reference proteome database (Uniprot, Taxon ID: 10090) with the manufacturer's default parameters. Briefly, trypsin/P was set as the digestion

enzyme, allowing for two missed cleavages. Cysteine carbamidomethylation was set as a fixed modification, while methionine oxidation and protein N-terminus acetylation were set as variable modifications. Identification was performed using a 1% q value cutoff at both the precursor and protein levels. Both peptide precursor and protein false discovery rates were controlled at 1%. Ion chromatograms of fragment ions were used for quantification, with the area under the curve between the XIC peak boundaries calculated for each targeted ion. DDA raw files were utilized in Library Extension Runs to enhance proteome coverage to generate a hybrid library. All PRM data analysis and integration were performed using Skyline software. The transitions' intensity rank order and chromatographic elution were required to match those of a synthetic standard for each measured peptide.

Differential abundance of proteins was analyzed similarly to House *et al.*[72] using the R v4.4.0 package limma (v3.60.0). Briefly, LIMMA-eBayes was fit on all proteins with less than 30% missingness and any remaining missing values were imputed using left-censored methods from imputeLCMD (v2.1). Second generation p values were then calculated using a null interval of 0.75-1.25 fold-differences to reduce the Type 1 Error rate and improved interpretability[75]. Gene set enrichment analysis (GSEA) on differentially abundant proteins was conducted using the gseGO function via clusterProfiler[76] (v4.12.0) and examined all of: biological process, cellular component, and molecular function. Significance of enrichment was based on Benjamini-Hochberg-adjusted p values[77]. Results of gseGO were visualized through network plots via the aPEAR package[78] (v1.0.0) and distinct pathway clusters from this analysis were used to calculate average normalized enrichment scores to represent overall enrichment in activated and suppressed pathways. The pipelines used for this analysis are hosted on GitHub: https://github.com/vari-bbc/Ugcg-KO_proteomics_analysis.

T cell killing assay

C57BL/6J mice were adoptively transferred with 1-5x10^5 Thy1.1$^+$CD8$^+$ OT-I cells (NTC- or sg*Ugcg*-modified) via the tail vein and infected with *Lm*-OVA the following day. At 7 dpi, Thy1.1$^+$ cells were rapidly isolated from the spleen using magnetic beads via positive selection. tdTomato-expressing MC38-OVA cells[16] were seeded in a 96-well plate (5x10^3 cells/well). 24 h later, a range of 2x10^5 to

~1563 *Lm*-OVA-activated NTC- or sg*Ugcg*-modified CD8$^+$ OT-I cells were added to the MC38-OVA cells in standard IMDM supplemented with 50 U/mL IL-2. tdTomato$^+$ cells were quantified over a 24 h period using IncuCyte live-cell analysis (Sartorius). The percentage of dead MC38-OVA tumor cells was calculated by normalizing the number of tdTomato-expressing cells to media-only (no T cell) controls.

B16-OVA tumor model and OT-I cell adoptive transfer

Female C57BL/6J mice were injected with 5x10^5 B16-OVA cells subcutaneously in the abdominal flank. Once palpable tumors were present, tumor measurements were obtained every 2-3 days using a caliper. 7 days after B16-OVA cell injection, mice received 1x10^6 Thy1.1$^+$CD8$^+$ OT-I cells (NTC- or sg*Ugcg*-modified) or HBSS as a vehicle control intravenously via the tail vein. Mice were euthanized as they reached human endpoints, which included a maximum tumor volume of $\geq$1500 mm^3. For tumor-infiltrating lymphocyte (TIL) analysis, tumors were harvested 14 days after B16-OVA cell injection (7 days after OT-I adoptive transfer) and mechanically disrupted to generate a single-cell suspension. Cells were pelleted (500 RCF for 5 min at 4°C) and resuspended in red blood cell lysis buffer (0.1 mM EDTA, 155 mM NH_4Cl, and 12 mM $NaHCO_3$) for 1 min at room temperature. Cells were stained and analyzed by flow cytometry as described in the "*Flow cytometry*" section.

TCR crosslinking and lipid raft aggregation analysis

Activated NTC- or sg*Ugcg*-modified CD8$^+$ T cells were starved of IL-2 for 4 hr. Cells were incubated with 10 μg/mL anti-CD3ε (clone 145-2C11) on ice for 30 min, and then with 10 μg/mL biotin-conjugated goat anti-Armenian hamster IgG at 37°C for 30 min. Sodium azide was added at a final concentration of 0.2% w/v to terminate the reaction. 10,000 cells in 100 μL of PBS were transferred to 13 mm single ring slides (Fisherbrand) using a Shandon Cytospin 3 centrifuge (1,000 RPM for 5 min). Cells were then fixed in 10% neutral-buffered formalin for 10 min at room temperature, washed twice with PBS (5 min each), and washed once with reverse osmosis (RO) water for 5 min. Slides were allowed to dry overnight at room temperature and then stored at 4°C until ready to stain.

Prior to staining, cells were washed twice with PBS (5 min each) and blocked with 2% FBS for 30 min at room temperature. Antibody/stain dilutions were performed using Antibody Diluent (Dako): CTxB-FITC (1:100) and streptavidin-Alexa Fluor 647 (1:500). Cells were stained overnight at 4°C. Cells were counterstained with DAPI for 10 min at room temperature prior to cover slip mounting with ProLonged Gold Antifade Mountant (Thermo Fisher). Slides were stored at 4°C (protected from light) until ready to image.

Confocal Z-stacks were collected using a Zeiss LSM 880 equipped with an Axio Observer 7 inverted microscope body and acquired with Zen Black (v2.3) software using 405 nm diode, 488 nm argon ion, and 633 nm HeNe laser lines, plus a transmitted light channel and a 0.92 AU pinhole. Emitted light was detected through a Zeiss Plan-apochromat 63x/1.4 NA oil immersion objective, using a PMT GaAsP detector. Images were collected sequentially at 1024x1024 pixel resolution, using 0.5 μm z-steps. Individual voxels were therefore 0.13 μm x 0.13 μm x 0.5 μm (xyz). A pixel dwell time of 0.42 μs and an optical zoom of 1.0 were used for the collection of all images. Large fields of view were obtained by automated collection and stitching of a 3x3 rectangular grid with 10% overlap.

Confocal Z-stacks were converted to max projections, channels split and saved as a TIFF using Fiji v2.15.1 prior to importing into CellProfiler for analysis[79,80]. The maximum projections for the DAPI, anti-streptavidin (CD3ε), and CTxB channels were used to quantify the number, location, and fluorescence distribution of the TCRs and lipid rafts per cell. Briefly, nuclei and their approximate cytoplasmic outlines were generated with the IdentifyPrimaryObjects and IdentifySecondaryObjects modules using the DAPI and CTxB channels, respectively. The objects from IdentifySecondaryObjects module were then used to mask the TCR channel; IdentifyPrimaryObjects module was used to segment the TCR puncta in this masked channel. Once all objects were generated and related to each other, a series of measurement modules were used to quantify fluorescence intensity, distribution, and texture, and shape and size of detected puncta. The CellProfiler pipeline used for this analysis is hosted on GitHub: https://github.com/vaioic/Published_Scripts. All measurements were exported to a CSV file for further statistical analysis. Representative images were generated using the QuickFigures Fiji plugin[81].

QUANTIFICATION AND STATISTICAL ANALYSIS

Unless otherwise stated, data are presented as mean ± standard deviation (SD) for technical replicates and mean ± standard error of the mean (SEM) for biological replicates. Observations from technical replicate data were reproduced in at least two independent experiments. Statistical analyses were performed using GraphPad Prism software (GraphPad). A two-tailed, unpaired Student's t-test was used to compare the means between two independent groups. All other statistical tests are specified in the corresponding figure legends. Statistical significance is indicated in all figures by the following annotations: *, $p < 0.05$; **, $p < 0.01$; ***, $p < 0.001$; ****, $p < 0.0001$; ns, not significant.

SUPPLEMENTAL INFORMATION

Document S1 (.pdf) – Figures S1-S6.

Table S1 (.csv) – Differentially expressed proteins in control and UGCG-deficient $CD8^+$ T cells, related to Figure 6.

Table S2 (.csv) – gseGO pathway analysis, related to Figure 6.

Table S3 (.xlsx) – ddMS2 inclusion list for ion paired metabolomics.

REFERENCES

1. Pearce, E.L., Poffenberger, M.C., Chang, C.-H., and Jones, R.G. (2013). Fueling immunity: insights into metabolism and lymphocyte function. Science *342*, 1242454.

2. MacIver, N.J., Michalek, R.D., and Rathmell, J.C. (2013). Metabolic regulation of T lymphocytes. Annu. Rev. Immunol. *31*, 259–283.

3. Geltink, R.K., Kyle, R.L., and Pearce, E.L. (2018). Unraveling the complex interplay between T cell metabolism and function. Annu. Rev. Immunol. *36*, 461–488.

4. Jacobs, S.R., Herman, C.E., Maciver, N.J., Wofford, J.A., Wieman, H.L., Hammen, J.J., and Rathmell, J.C. (2008). Glucose uptake is limiting in T cell activation and requires CD28-mediated Akt-dependent and independent pathways. J. Immunol. *180*, 4476–4486.

5. Macintyre, A.N., Gerriets, V.A., Nichols, A.G., Michalek, R.D., Rudolph, M.C., Deoliveira, D., Anderson, S.M., Abel, E.D., Chen, B.J., Hale, L.P., et al. (2014). The glucose transporter Glut1 is selectively essential for CD4 T cell activation and effector function. Cell Metab. *20*, 61–72.

6. Fu, H., Vuononvirta, J., Fanti, S., Bonacina, F., D'Amati, A., Wang, G., Poobalasingam, T., Fankhaenel, M., Lucchesi, D., Coleby, R., et al. (2023). The glucose transporter 2 regulates CD8+ T cell function via environment sensing. Nat. Metab. *5*, 1969–1985.

7. Chang, C.-H., Curtis, J.D., Maggi, L.B., Jr, Faubert, B., Villarino, A.V., O'Sullivan, D., Huang, S.C.-C., van der Windt, G.J.W., Blagih, J., Qiu, J., et al. (2013). Posttranscriptional control of T cell effector function by aerobic glycolysis. Cell *153*, 1239–1251.

8. Menk, A.V., Scharping, N.E., Moreci, R.S., Zeng, X., Guy, C., Salvatore, S., Bae, H., Xie, J., Young, H.A., Wendell, S.G., et al. (2018). Early TCR signaling induces rapid aerobic glycolysis enabling distinct acute T cell effector functions. Cell Rep. *22*, 1509–1521.

9. Ma, E.H., Verway, M.J., Johnson, R.M., Roy, D.G., Steadman, M., Hayes, S., Williams, K.S., Sheldon, R.D., Samborska, B., Kosinski, P.A., et al. (2019). Metabolic Profiling Using Stable Isotope Tracing Reveals Distinct Patterns of Glucose Utilization by Physiologically Activated CD8+ T Cells. Immunity *51*, 856-870.e5.

10. Cham, C.M., and Gajewski, T.F. (2005). Glucose availability regulates IFN-gamma production and p70S6 kinase activation in CD8+ effector T cells. J. Immunol. *174*, 4670–4677.

11. Cham, C.M., Driessens, G., O'Keefe, J.P., and Gajewski, T.F. (2008). Glucose deprivation inhibits multiple key gene expression events and effector functions in CD8+ T cells. Eur. J. Immunol. *38*, 2438–2450.

12. MacIver, N.J., Jacobs, S.R., Wieman, H.L., Wofford, J.A., Coloff, J.L., and Rathmell, J.C. (2008). Glucose metabolism in lymphocytes is a regulated process with significant effects on immune cell function and survival. J. Leukoc. Biol. *84*, 949–957.

13. Blagih, J., Coulombe, F., Vincent, E.E., Dupuy, F., Galicia-Vázquez, G., Yurchenko, E., Raissi, T.C., van der Windt, G.J.W., Viollet, B., Pearce, E.L., et al. (2015). The energy sensor AMPK regulates T cell metabolic adaptation and effector responses in vivo. Immunity *42*, 41–54.

14. Sena, L.A., Li, S., Jairaman, A., Prakriya, M., Ezponda, T., Hildeman, D.A., Wang, C.-R., Schumacker, P.T., Licht, J.D., Perlman, H., et al. (2013). Mitochondria are required for antigen-specific T cell activation through reactive oxygen species signaling. Immunity *38*, 225–236.

15. Kaymak, I., Luda, K.M., Duimstra, L.R., Ma, E.H., Longo, J., Dahabieh, M.S., Faubert, B., Oswald, B.M., Watson, M.J., Kitchen-Goosen, S.M., et al. (2022). Carbon source availability drives nutrient utilization in CD8+ T cells. Cell Metab. *34*, 1298-1311.e6.

16. Luda, K.M., Longo, J., Kitchen-Goosen, S.M., Duimstra, L.R., Ma, E.H., Watson, M.J., Oswald, B.M., Fu, Z., Madaj, Z., Kupai, A., et al. (2023). Ketolysis drives CD8+ T cell effector function through effects on histone acetylation. Immunity *56*, 2021-2035.e8.

17. Ma, E.H., Dahabieh, M.S., DeCamp, L.M., Kaymak, I., Kitchen-Goosen, S.M., Oswald, B.M., Longo, J., Roy, D.G., Verway, M.J., Johnson, R.M., et al. (2024). ^{13}C metabolite tracing reveals glutamine and acetate as critical in vivo fuels for CD8 T cells. Sci Adv *10*, eadj1431.

18. Edwards-Hicks, J., Apostolova, P., Buescher, J.M., Maib, H., Stanczak, M.A., Corrado, M., Klein Geltink, R.I., Maccari, M.E., Villa, M., Carrizo, G.E., et al. (2023). Phosphoinositide acyl chain saturation drives CD8+ effector T cell signaling and function. Nat. Immunol. *24*, 516–530.

19. Sheldon, R.D., Ma, E.H., DeCamp, L.M., Williams, K.S., and Jones, R.G. (2021). Interrogating in vivo T-cell metabolism in mice using stable isotope labeling metabolomics and rapid cell sorting. Nat. Protoc. *16*, 4494–4521.

20. Ma, R., Ji, T., Zhang, H., Dong, W., Chen, X., Xu, P., Chen, D., Liang, X., Yin, X., Liu, Y., et al. (2018). A Pck1-directed glycogen metabolic program regulates formation and maintenance of memory CD8+ T cells. Nat. Cell Biol. *20*, 21–27.

21. Zhang, H., Liu, J., Yang, Z., Zeng, L., Wei, K., Zhu, L., Tang, L., Wang, D., Zhou, Y., Lv, J., et al. (2022). TCR activation directly stimulates PYGB-dependent glycogenolysis to fuel the early recall response in CD8+ memory T cells. Mol. Cell *82*, 3077-3088.e6.

22. Longo, J., Watson, M.J., Vos, M.J., Williams, K.S., and Jones, R.G. (2022). PYGBacking on glycogen metabolism to fuel early memory T cell recall responses. Mol. Cell *82*, 2918–2921.

23. Amado, M., Almeida, R., Schwientek, T., and Clausen, H. (1999). Identification and characterization of large galactosyltransferase gene families: galactosyltransferases for all functions. Biochim. Biophys. Acta *1473*, 35–53.

24. Hennet, T. (2002). The galactosyltransferase family. Cell. Mol. Life Sci. *59*, 1081–1095.

25. Asano, M., Furukawa, K., Kido, M., Matsumoto, S., Umesaki, Y., Kochibe, N., and Iwakura, Y. (1997). Growth retardation and early death of β-1, 4-galactosyltransferase knockout mice with augmented proliferation and abnormal differentiation of epithelial cells. EMBO J. *16*, 1850–1857.

26. Tokuda, N., Numata, S., Li, X., Nomura, T., Takizawa, M., Kondo, Y., Yamashita, Y., Hashimoto, N., Kiyono, T., Urano, T., et al. (2013). β4GalT6 is involved in the synthesis of lactosylceramide with less intensity than β4GalT5. Glycobiology *23*, 1175–1183.

27. Yoshihara, T., Satake, H., Nishie, T., Okino, N., Hatta, T., Otani, H., Naruse, C., Suzuki, H., Sugihara, K., Kamimura, E., et al. (2018). Lactosylceramide synthases encoded by B4galt5 and 6 genes are pivotal for neuronal generation and myelin formation in mice. PLoS Genet. *14*, e1007545.

28. Breitling, J., and Aebi, M. (2013). N-linked protein glycosylation in the endoplasmic reticulum. Cold Spring Harb. Perspect. Biol. *5*, a013359.

29. Williams, R.V., Guay, K.P., Hurlbut Lesk, O.A., Clerico, E.M., Hebert, D.N., and Gierasch, L.M. (2024). Insights into the interaction between UGGT, the gatekeeper of folding in the ER, and its partner, the selenoprotein SEP15. Proc. Natl. Acad. Sci. U. S. A. *121*, e2315009121.

30. Bojar, D., Meche, L., Meng, G., Eng, W., Smith, D.F., Cummings, R.D., and Mahal, L.K. (2022). A useful guide to lectin binding: Machine-learning directed annotation of 57 unique lectin specificities. ACS Chem. Biol. *17*, 2993–3012.

31. Stanley, P., Moremen, K.W., Lewis, N.E., Taniguchi, N., and Aebi, M. (2022). N-Glycans. In Essentials of Glycobiology (Cold Spring Harbor Laboratory Press), pp. 103–116.

32. Li, L., Guan, W., Zhang, G., Wu, Z., Yu, H., Chen, X., and Wang, P.G. (2020). Microarray analyses of closely related glycoforms reveal different accessibilities of glycan determinants on N-glycan branches. Glycobiology *30*, 334–345.

33. Klamer, Z.L., Harris, C.M., Beirne, J.M., Kelly, J.E., Zhang, J., and Haab, B.B. (2022). CarboGrove: a resource of glycan-binding specificities through analyzed glycan-array datasets from all platforms. Glycobiology *32*, 679–690.

34. Fishman, P.H., and Brady, R.O. (1976). Biosynthesis and Function of Gangliosides. Science, New Series *194*, 906–915.

35. McEachern, K.A., Fung, J., Komarnitsky, S., Siegel, C.S., Chuang, W.-L., Hutto, E., Shayman, J.A., Grabowski, G.A., Aerts, J.M.F.G., Cheng, S.H., et al. (2007). A specific and potent inhibitor of glucosylceramide synthase for substrate inhibition therapy of Gaucher disease. Mol. Genet. Metab. *91*, 259–267.

36. Sonnino, S., Mauri, L., Chigorno, V., and Prinetti, A. (2007). Gangliosides as components of lipid membrane domains. Glycobiology *17*, 1R-13R.

37. Janes, P.W., Ley, S.C., and Magee, A.I. (1999). Aggregation of lipid rafts accompanies signaling via the T cell antigen receptor. J. Cell Biol. *147*, 447–461.

38. Dupré, L., Aiuti, A., Trifari, S., Martino, S., Saracco, P., Bordignon, C., and Roncarolo, M. (2002). Wiskott-Aldrich syndrome protein regulates lipid raft dynamics during immunological synapse formation. Immunity *17*, 157–166.

39. Kuziemko, G.M., Stroh, M., and Stevens, R.C. (1996). Cholera Toxin Binding Affinity and Specificity for Gangliosides Determined by Surface Plasmon Resonance. Biochemistry *35*, 6375–6384.

40. Day, C.A., and Kenworthy, A.K. (2015). Functions of cholera toxin B-subunit as a raft cross-linker. Essays Biochem. *57*, 135–145.

41. Ma, E.H., Bantug, G., Griss, T., Condotta, S., Johnson, R.M., Samborska, B., Mainolfi, N., Suri, V., Guak, H., Balmer, M.L., et al. (2017). Serine Is an Essential Metabolite for Effector T Cell Expansion. Cell Metab. *25*, 345–357.

42. Qiu, J., Villa, M., Sanin, D.E., Buck, M.D., O'Sullivan, D., Ching, R., Matsushita, M., Grzes, K.M., Winkler, F., Chang, C.-H., et al. (2019). Acetate promotes T cell effector function during glucose restriction. Cell Rep. *27*, 2063-2074.e5.

43. Kaymak, I., Watson, M.J., Oswald, B.M., Ma, S., Johnson, B.K., DeCamp, L.M., Mabvakure, B.M., Luda, K.M., Ma, E.H., Lau, K., et al. (2024). ACLY and ACSS2 link nutrient-dependent chromatin accessibility to CD8 T cell effector responses. J. Exp. Med. *221*, e20231820.

44. Karagiannis, F., Peukert, K., Surace, L., Michla, M., Nikolka, F., Fox, M., Weiss, P., Feuerborn, C., Maier, P., Schulz, S., et al. (2022). Impaired ketogenesis ties metabolism to T cell dysfunction in COVID-19. Nature *609*, 801–807.

45. Cantor, J.R., Abu-Remaileh, M., Kanarek, N., Freinkman, E., Gao, X., Louissaint, A., Lewis, C.A., and Sabatini, D.M. (2017). Physiologic Medium Rewires Cellular Metabolism and Reveals Uric Acid as an Endogenous Inhibitor of UMP Synthase. Cell *169*, 258–272.

46. Sullivan, M.R., Danai, L.V., Lewis, C.A., Chan, S.H., Gui, D.Y., Kunchok, T., Dennstedt, E.A., Vander Heiden, M.G., Muir, A., Heiden, M.G.V., et al. (2019). Quantification of microenvironmental metabolites in murine cancers reveals determinants of tumor nutrient availability. Elife *8*, e44235.

47. Hui, S., Ghergurovich, J.M., Morscher, R.J., Jang, C., Teng, X., Lu, W., Esparza, L.A., Reya, T., Le Zhan, L., Yanxiang Guo, J., et al. (2017). Glucose feeds the TCA cycle via circulating lactate. Nature *551*, 115–118.

48. Swamy, M., Pathak, S., Grzes, K.M., Damerow, S., Sinclair, L.V., van Aalten, D.M.F., and Cantrell, D.A. (2016). Glucose and glutamine fuel protein O-GlcNAcylation to control T cell self-renewal and malignancy. Nat. Immunol. *17*, 712–720.

49. Comelli, E.M., Sutton-Smith, M., Yan, Q., Amado, M., Panico, M., Gilmartin, T., Whisenant, T., Lanigan, C.M., Head, S.R., Goldberg, D., et al. (2006). Activation of murine CD4+ and CD8+ T lymphocytes leads to dramatic remodeling of N-linked glycans. J. Immunol. *177*, 2431–2440.

50. Chen, H.-L., Li, C.F., Grigorian, A., Tian, W., and Demetriou, M. (2009). T cell receptor signaling co-regulates multiple Golgi genes to enhance N-glycan branching. J. Biol. Chem. *284*, 32454–32461.

51. Demetriou, M., Granovsky, M., Quaggin, S., and Dennis, J.W. (2001). Negative regulation of T-cell activation and autoimmunity by Mgat5 N-glycosylation. Nature *409*, 733–739.

52. Morgan, R., Gao, G., Pawling, J., Dennis, J.W., Demetriou, M., and Li, B. (2004). N-acetylglucosaminyltransferase V (Mgat5)-mediated N-glycosylation negatively regulates Th1 cytokine production by T cells. J. Immunol. *173*, 7200–7208.

53. Toscano, M.A., Bianco, G.A., Ilarregui, J.M., Croci, D.O., Correale, J., Hernandez, J.D., Zwirner, N.W., Poirier, F., Riley, E.M., Baum, L.G., et al. (2007). Differential glycosylation of TH1, TH2 and TH-17 effector cells selectively regulates susceptibility to cell death. Nat. Immunol. *8*, 825–834.

54. Nagafuku, M., Okuyama, K., Onimaru, Y., Suzuki, A., Odagiri, Y., Yamashita, T., Iwasaki, K., Fujiwara, M., Takayanagi, M., Ohno, I., et al. (2012). CD4 and CD8 T cells require different membrane gangliosides for activation. Proc. Natl. Acad. Sci. U. S. A. *109*, E336-42.

55. Izzati, F.N., Choksi, H., Giuliana, P., Abd-Rabbo, D., Elsaesser, H., Blundell, A., Affe, V., Kannen, V., Jame-Chenarboo, Z., Schmidt, E., et al. (2024). A Unified Atlas of T cell Glycophysiology. bioRxiv. https://doi.org/10.1101/2024.08.24.609521.

56. Gómez-Móuton, C., Abad, J.L., Mira, E., Lacalle, R.A., Gallardo, E., Jiménez-Baranda, S., Illa, I., Bernad, A., Mañes, S., and Martínez-A, C. (2001). Segregation of leading-edge and uropod components into specific lipid rafts during T cell polarization. Proc. Natl. Acad. Sci. U. S. A. *98*, 9642–9647.

57. Cho, J.-H., Kim, H.-O., Surh, C.D., and Sprent, J. (2010). T cell receptor-dependent regulation of lipid rafts controls naive CD8+ T cell homeostasis. Immunity *32*, 214–226.

58. Marwali, M.R., MacLeod, M.A., Muzia, D.N., and Takei, F. (2004). Lipid rafts mediate association of LFA-1 and CD3 and formation of the immunological synapse of CTL. J. Immunol. *173*, 2960–2967.

59. Ichikawa, S., Nakajo, N., Sakiyama, H., and Hirabayashi, Y. (1994). A mouse B16 melanoma mutant deficient in glycolipids. Proc. Natl. Acad. Sci. U. S. A. *91*, 2703–2707.

60. Yamashita, T., Wada, R., Sasaki, T., Deng, C., Bierfreund, U., Sandhoff, K., and Proia, R.L. (1999). A vital role for glycosphingolipid synthesis during development and differentiation. Proc. Natl. Acad. Sci. U. S. A. *96*, 9142–9147.

61. Liu, J., van der Hoeven, R., Kattan, W.E., Chang, J.T., Montufar-Solis, D., Chen, W., Wong, M., Zhou, Y., Lebrilla, C.B., and Hancock, J.F. (2023). Glycolysis regulates KRAS plasma membrane localization and function through defined glycosphingolipids. Nat. Commun. *14*, 465.

62. Soula, M., Unlu, G., Welch, R., Chudnovskiy, A., Uygur, B., Shah, V., Alwaseem, H., Bunk, P., Subramanyam, V., Yeh, H.-W., et al. (2024). Glycosphingolipid synthesis mediates immune evasion in KRAS-driven cancer. Nature *633*, 451–458.

63. Dong, L., Cao, Z., Chen, M., Liu, Y., Ma, X., Lu, Y., Zhang, Y., Feng, K., Zhang, Y., Meng, Z., et al. (2024). Inhibition of glycosphingolipid synthesis with eliglustat in combination with immune checkpoint inhibitors in advanced cancers: preclinical evidence and phase I clinical trial. Nat. Commun. *15*, 6970.

64. Haring, J.S., Corbin, G.A., and Harty, J.T. (2005). Dynamic regulation of IFN-gamma signaling in antigen-specific CD8+ T cells responding to infection. J. Immunol. *174*, 6791–6802.

65. Cordeiro, B., Jeon, P., Boukhaled, G.M., Corrado, M., Lapohos, O., Roy, D.G., Williams, K., Jones, R.G., Gruenheid, S., Sagan, S.M., et al. (2020). MicroRNA-9 fine-tunes dendritic cell function by suppressing negative regulators in a cell-type-specific manner. Cell Rep. *31*, 107585.

66. Chen, R., Bélanger, S., Frederick, M.A., Li, B., Johnston, R.J., Xiao, N., Liu, Y.-C., Sharma, S., Peters, B., Rao, A., et al. (2014). In vivo RNA interference screens identify regulators of antiviral CD4(+) and CD8(+) T cell differentiation. Immunity *41*, 325–338.

67. Nüssing, S., House, I.G., Kearney, C.J., Chen, A.X.Y., Vervoort, S.J., Beavis, P.A., Oliaro, J., Johnstone, R.W., Trapani, J.A., and Parish, I.A. (2020). Efficient CRISPR/Cas9 gene editing in uncultured naive mouse T cells for in vivo studies. J. Immunol. *204*, 2308–2315.

68. Desjardins, J., Cowan, M., and Yamanaka, Y. (2022). Designing Genetically Engineered Mouse Models (GEMMs) Using CRISPR Mediated Genome Editing. Methods Mol Biol *2429*, 515–531.

69. Guak, H., Weiland, M., Ark, A.V., Zhai, L., Lau, K., Corrado, M., Davidson, P., Asiedu, E., Mabvakure, B., Compton, S., et al. (2024). Transcriptional programming mediated by the histone demethylase KDM5C regulates dendritic cell population heterogeneity and function. Cell Rep. *43*, 114506.

70. Mookerjee, S.A., Gerencser, A.A., Nicholls, D.G., and Brand, M.D. (2017). Quantifying intracellular rates of glycolytic and oxidative ATP production and consumption using extracellular flux measurements. J. Biol. Chem. *292*, 7189–7207.

71. Bligh, E.G., and Dyer, W.J. (1959). A rapid method of total lipid extraction and purification. Can. J. Biochem. Physiol. *37*, 911–917.

72. House, R.R.J., Soper-Hopper, M.T., Vincent, M.P., Ellis, A.E., Capan, C.D., Madaj, Z.B., Wolfrum, E., Isaguirre, C.N., Castello, C.D., Johnson, A.B., et al. (2024). A diverse proteome is present and enzymatically active in metabolite extracts. Nat. Commun. *15*, 5796.

73. Heinrich, P., Kohler, C., Ellmann, L., Kuerner, P., Spang, R., Oefner, P.J., and Dettmer, K. (2018). Correcting for natural isotope abundance and tracer impurity in MS-, MS/MS- and high-resolution-multiple-tracer-data from stable isotope labeling experiments with IsoCorrectoR. Sci. Rep. *8*, 17910.

74. Sokol, K.H., Lee, C.J., Rogers, T.J., Waldhart, A., Ellis, A.E., Madireddy, S., Daniels, S.R., Ye, X., Olesnavich, M., Johnson, A., et al. (2024). Lipid availability influences ferroptosis sensitivity in cancer cells by regulating polyunsaturated fatty acid trafficking. bioRxiv. https://doi.org/10.1101/2024.05.06.592780.

75. Blume, J.D., D'Agostino McGowan, L., Dupont, W.D., and Greevy, R.A., Jr (2018). Second-generation p-values: Improved rigor, reproducibility, & transparency in statistical analyses. PLoS One *13*, e0188299.

76. Wu, T., Hu, E., Xu, S., Chen, M., Guo, P., Dai, Z., Feng, T., Zhou, L., Tang, W., Zhan, L., et al. (2021). clusterProfiler 4.0: A universal enrichment tool for interpreting omics data. Innovation (Camb) *2*, 100141.

77. Subramanian, A., Tamayo, P., Mootha, V.K., Mukherjee, S., Ebert, B.L., Gillette, M.A., Paulovich, A., Pomeroy, S.L., Golub, T.R., Lander, E.S., et al. (2005). Gene set enrichment analysis: a knowledge-based approach for interpreting genome-wide expression profiles. Proc. Natl. Acad. Sci. U. S. A. *102*, 15545–15550.

78. Kerseviciute, I., and Gordevicius, J. (2023). aPEAR : an R package for autonomous visualization of pathway enrichment networks. Bioinformatics *39*, btad672.

79. Schindelin, J., Arganda-Carreras, I., Frise, E., Kaynig, V., Longair, M., Pietzsch, T., Preibisch, S., Rueden, C., Saalfeld, S., Schmid, B., et al. (2012). Fiji: an open-source platform for biological-image analysis. Nat. Methods *9*, 676–682.

80. Stirling, D.R., Swain-Bowden, M.J., Lucas, A.M., Carpenter, A.E., Cimini, B.A., and Goodman, A. (2021). CellProfiler 4: improvements in speed, utility and usability. BMC Bioinformatics *22*, 433.

81. Mazo, G. (2021). QuickFigures: A toolkit and ImageJ PlugIn to quickly transform microscope images into scientific figures. PLoS One *16*, e0240280.

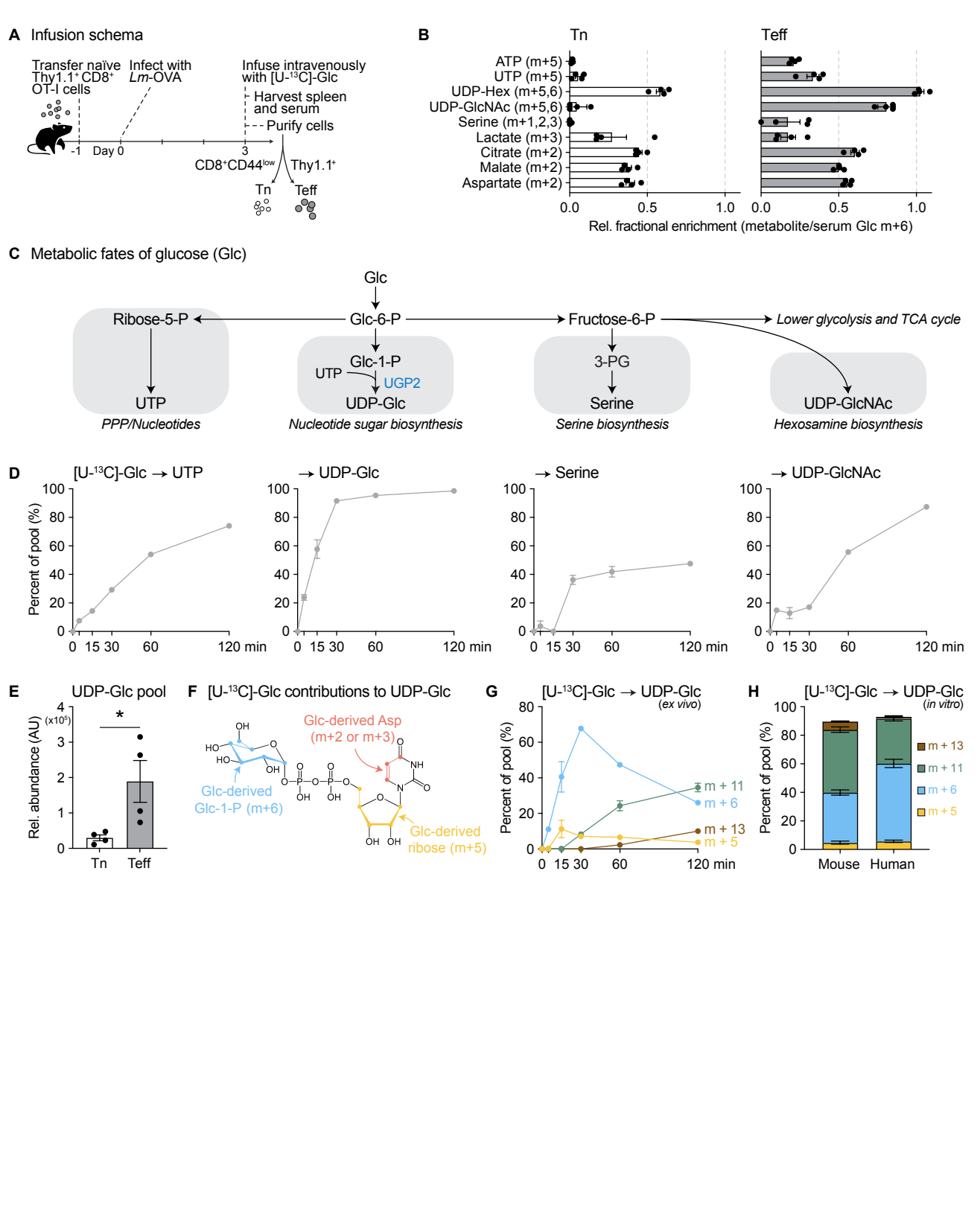
A Infusion schema
Transfer naïve Thy1.1+ CD8+ OT-I cells
Infect with Lm-OVA
Infuse intravenously with [U-13C]-Glc
Harvest spleen and serum
Purify cells
-1
Day 0
3
CD8+CD44low
Thy1.1+
Tn
Teff
B
Tn
Teff
ATP (m+5)
UTP (m+5)
UDP-Hex (m+5,6)
UDP-GlcNAc (m+5,6)
Serine (m+1,2,3)
Lactate (m+3)
Citrate (m+2)
Malate (m+2)
Aspartate (m+2)
0.0
0.5
1.0
Rel. fractional enrichment (metabolite/serum Glc m+6)
C Metabolic fates of glucose (Glc)
Glc
Ribose-5-P
Glc-6-P
Fructose-6-P
Lower glycolysis and TCA cycle
UTP
PPP/Nucleotides
Glc-1-P
UTP
UGP2
UDP-Glc
Nucleotide sugar biosynthesis
3-PG
Serine
Serine biosynthesis
UDP-GlcNAc
Hexosamine biosynthesis
D
[U-13C]-Glc → UTP
→ UDP-Glc
→ Serine
→ UDP-GlcNAc
Percent of pool (%)
0 15 30 60 120 min
E
UDP-Glc pool
Rel. abundance (AU)
(x10^5)
*
Tn
Teff
F
[U-13C]-Glc contributions to UDP-Glc
Glc-derived Asp (m+2 or m+3)
Glc-derived Glc-1-P (m+6)
Glc-derived ribose (m+5)
G
[U-13C]-Glc → UDP-Glc (ex vivo)
Percent of pool (%)
m + 11
m + 6
m + 13
m + 5
0 15 30 60 120 min
H
[U-13C]-Glc → UDP-Glc (in vitro)
Percent of pool (%)
m + 13
m + 11
m + 6
m + 5
Mouse
Human

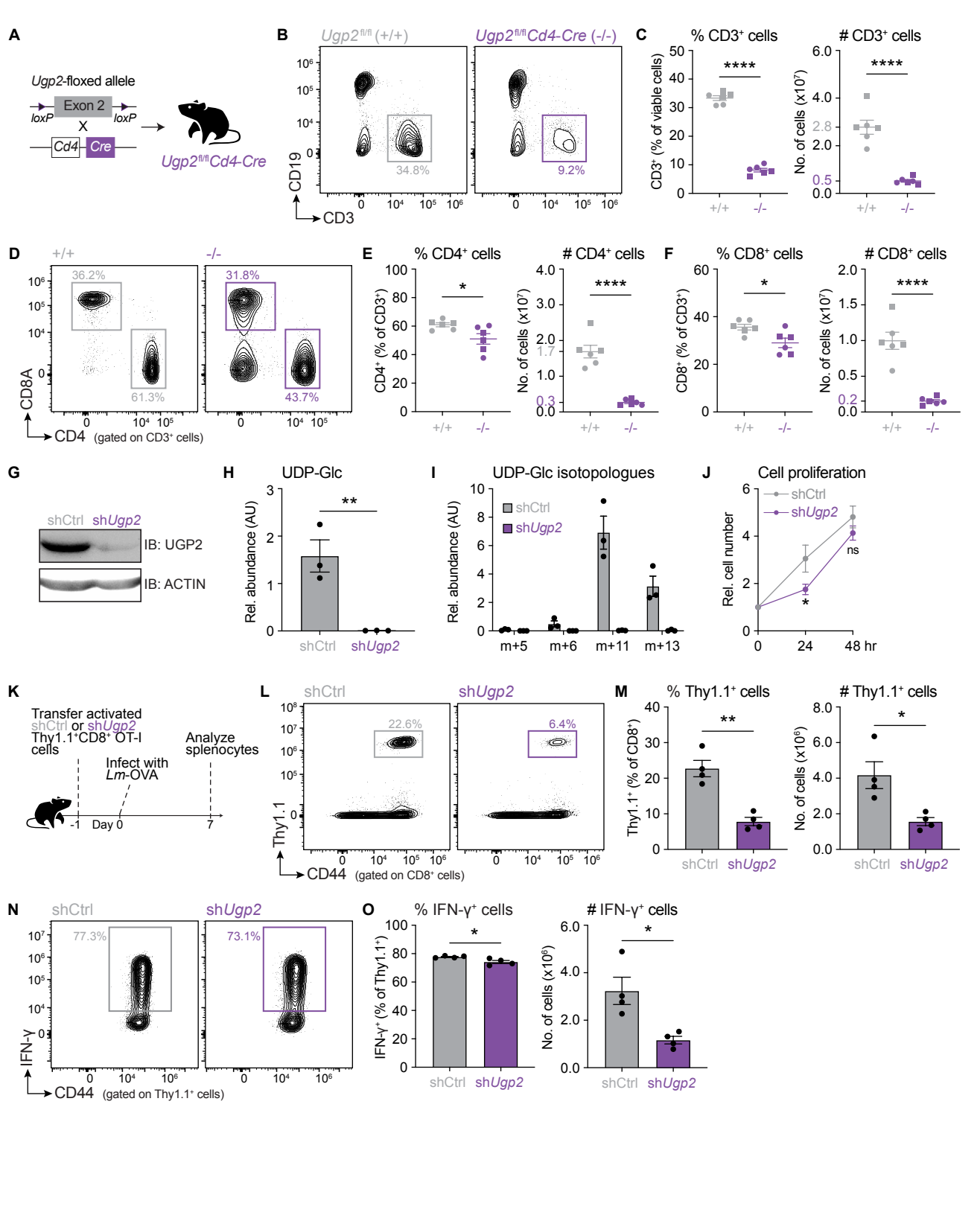
A
Ugp2-floxed allele
Exon 2
loxP
loxP
X
Cd4
Cre
Ugp2fl/flCd4-Cre
B
Ugp2fl/fl (+/+)
Ugp2fl/flCd4-Cre (-/-)
CD19
CD3
34.8%
9.2%
C
% CD3+ cells
# CD3+ cells
CD3+ (% of viable cells)
No. of cells (x10^7)
****
****
+/+
-/-
D
+/+
-/-
36.2%
61.3%
31.8%
43.7%
CD8A
CD4 (gated on CD3+ cells)
E
% CD4+ cells
# CD4+ cells
CD4+ (% of CD3+)
No. of cells (x10^7)
*
****
F
% CD8+ cells
# CD8+ cells
CD8+ (% of CD3+)
No. of cells (x10^7)
*
****
G
shCtrl
shUgp2
IB: UGP2
IB: ACTIN
H
UDP-Glc
Rel. abundance (AU)
**
shCtrl
shUgp2
I
UDP-Glc isotopologues
Rel. abundance (AU)
shCtrl
shUgp2
m+5
m+6
m+11
m+13
J
Cell proliferation
shCtrl
shUgp2
Rel. cell number
ns
*
0
24
48 hr
K
Transfer activated
shCtrl or shUgp2
Thy1.1+CD8+ OT-I
cells
Infect with
Lm-OVA
Analyze
splenocytes
-1
Day 0
7
L
shCtrl
shUgp2
22.6%
6.4%
Thy1.1
CD44 (gated on CD8+ cells)
M
% Thy1.1+ cells
# Thy1.1+ cells
Thy1.1+ (% of CD8+)
No. of cells (x10^6)
**
*
shCtrl
shUgp2
N
shCtrl
shUgp2
77.3%
73.1%
IFN-γ
CD44 (gated on Thy1.1+ cells)
O
% IFN-γ+ cells
# IFN-γ+ cells
IFN-γ+ (% of Thy1.1+)
No. of cells (x10^6)
*
*
shCtrl
shUgp2

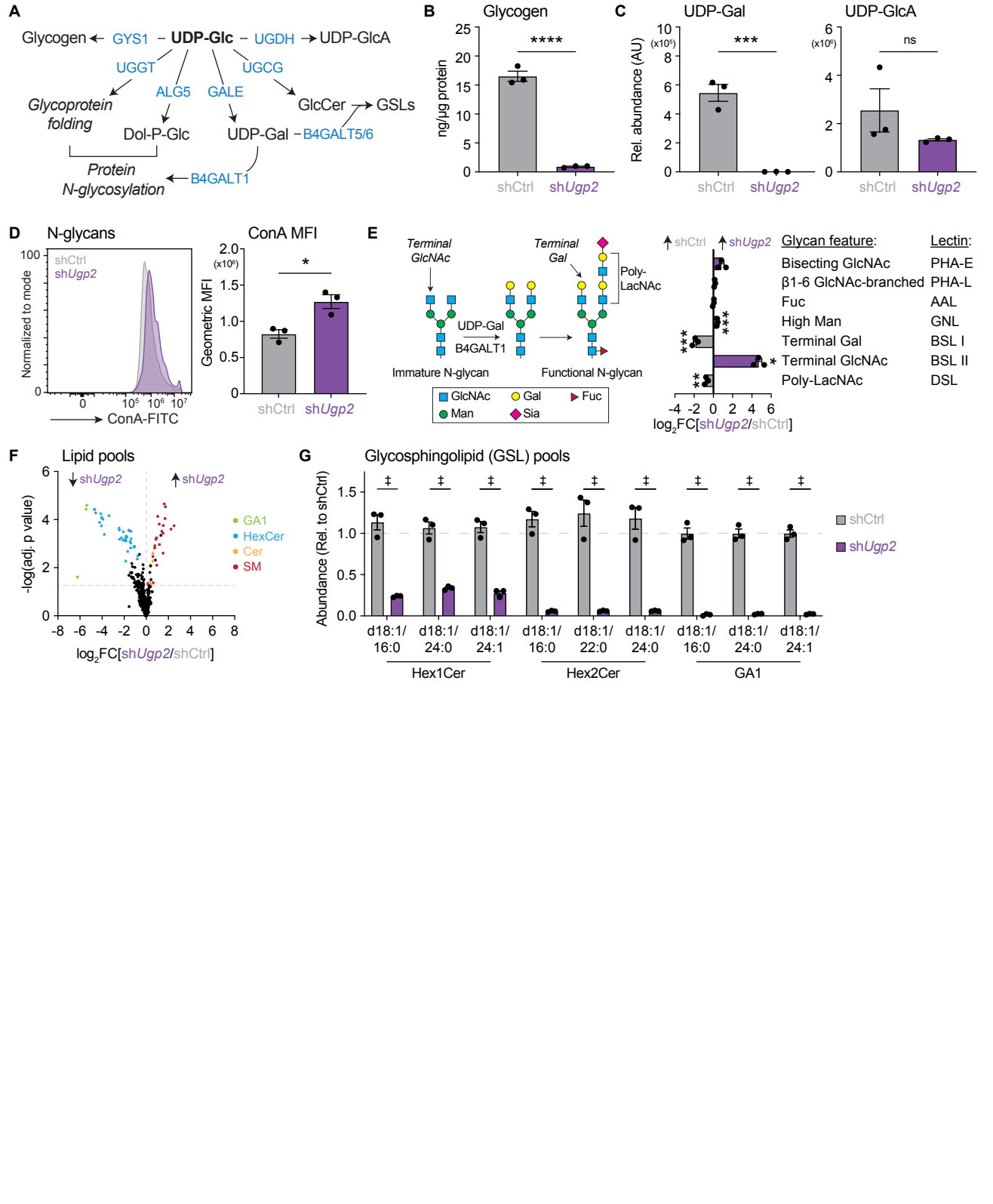
A
Glycogen
GYS1
UDP-Glc
UGDH
UDP-GlcA
UGGT
UGCG
ALG5
GALE
Glycoprotein folding
GlcCer
GSLs
Dol-P-Glc
UDP-Gal
B4GALT5/6
Protein N-glycosylation
B4GALT1
B
Glycogen
ng/µg protein
****
shCtrl
shUgp2
C
UDP-Gal
Rel. abundance (AU)
(x10⁵)
***
UDP-GlcA
(x10⁶)
ns
shCtrl
shUgp2
D
N-glycans
shCtrl
shUgp2
Normalized to mode
ConA-FITC
ConA MFI
Geometric MFI
(x10⁶)
*
shCtrl
shUgp2
E
Terminal GlcNAc
Terminal Gal
Poly-LacNAc
UDP-Gal
B4GALT1
Immature N-glycan
Functional N-glycan
GlcNAc
Gal
Fuc
Man
Sia
shCtrl
shUgp2
log2FC[shUgp2/shCtrl]
Glycan feature:
Lectin:
Bisecting GlcNAc
PHA-E
β1-6 GlcNAc-branched
PHA-L
Fuc
AAL
High Man
GNL
Terminal Gal
BSL I
Terminal GlcNAc
BSL II
Poly-LacNAc
DSL
F
Lipid pools
shUgp2
shUgp2
-log(adj. p value)
GA1
HexCer
Cer
SM
log2FC[shUgp2/shCtrl]
G
Glycosphingolipid (GSL) pools
Abundance (Rel. to shCtrl)
shCtrl
shUgp2
d18:1/16:0
d18:1/24:0
d18:1/24:1
d18:1/16:0
d18:1/22:0
d18:1/24:0
d18:1/16:0
d18:1/24:0
d18:1/24:1
Hex1Cer
Hex2Cer
GA1

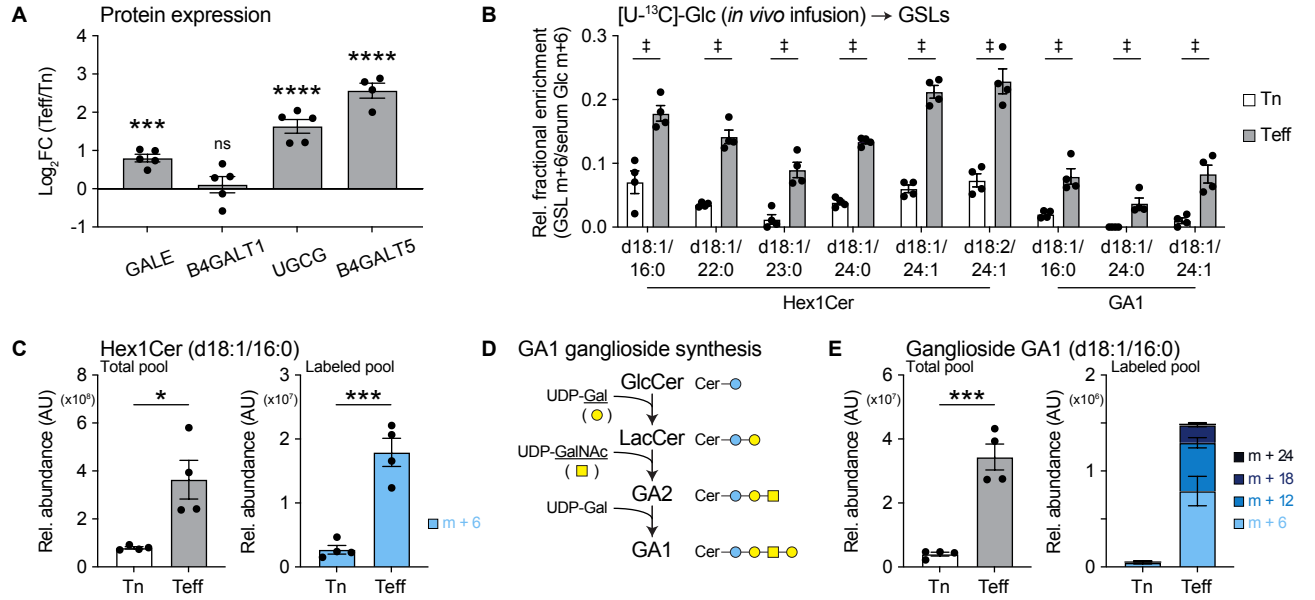
A
Protein expression
Log2FC (Teff/Tn)
***
ns
****
****
GALE
B4GALT1
UGCG
B4GALT5
B
[U-13C]-Glc (in vivo infusion) → GSLs
Rel. fractional enrichment (GSL m+6/serum Glc m+6)
Tn
Teff
d18:1/16:0
d18:1/22:0
d18:1/23:0
d18:1/24:0
d18:1/24:1
d18:2/24:1
d18:1/16:0
d18:1/24:0
d18:1/24:1
Hex1Cer
GA1
C
Hex1Cer (d18:1/16:0)
Total pool
Labeled pool
Rel. abundance (AU)
m + 6
D
GA1 ganglioside synthesis
UDP-Gal
GlcCer
LacCer
UDP-GalNAc
GA2
GA1
Cer
E
Ganglioside GA1 (d18:1/16:0)
m + 24
m + 18
m + 12
m + 6

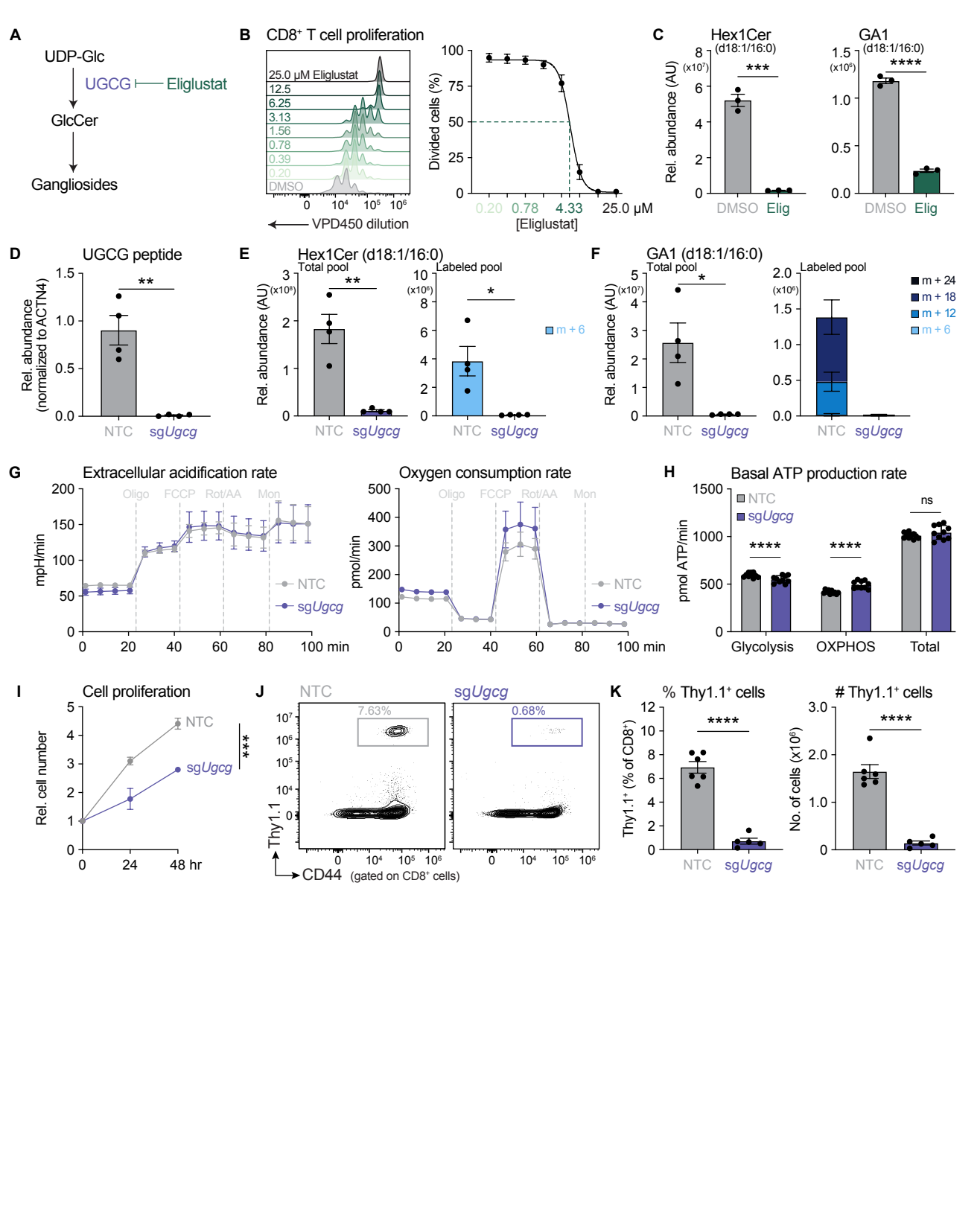
A
UDP-Glc
UGCG
Eliglustat
GlcCer
Gangliosides
B
CD8⁺ T cell proliferation
25.0 μM Eliglustat
12.5
6.25
3.13
1.56
0.78
0.39
0.20
DMSO
VPD450 dilution
Divided cells (%)
0.20 0.78 4.33 25.0 μM
[Eliglustat]
C
Hex1Cer (d18:1/16:0)
GA1 (d18:1/16:0)
Rel. abundance (AU)
DMSO Elig
D
UGCG peptide
Rel. abundance (normalized to ACTN4)
NTC sgUgcg
E
Hex1Cer (d18:1/16:0)
Total pool
Labeled pool
m + 6
F
GA1 (d18:1/16:0)
m + 24
m + 18
m + 12
m + 6
G
Extracellular acidification rate
Oligo FCCP Rot/AA Mon
mpH/min
Oxygen consumption rate
pmol/min
100 min
H
Basal ATP production rate
pmol ATP/min
Glycolysis OXPHOS Total
ns
I
Cell proliferation
Rel. cell number
48 hr
J
7.63%
0.68%
Thy1.1
CD44
(gated on CD8⁺ cells)
K
% Thy1.1⁺ cells
# Thy1.1⁺ cells
Thy1.1⁺ (% of CD8⁺)
No. of cells (x10⁶)

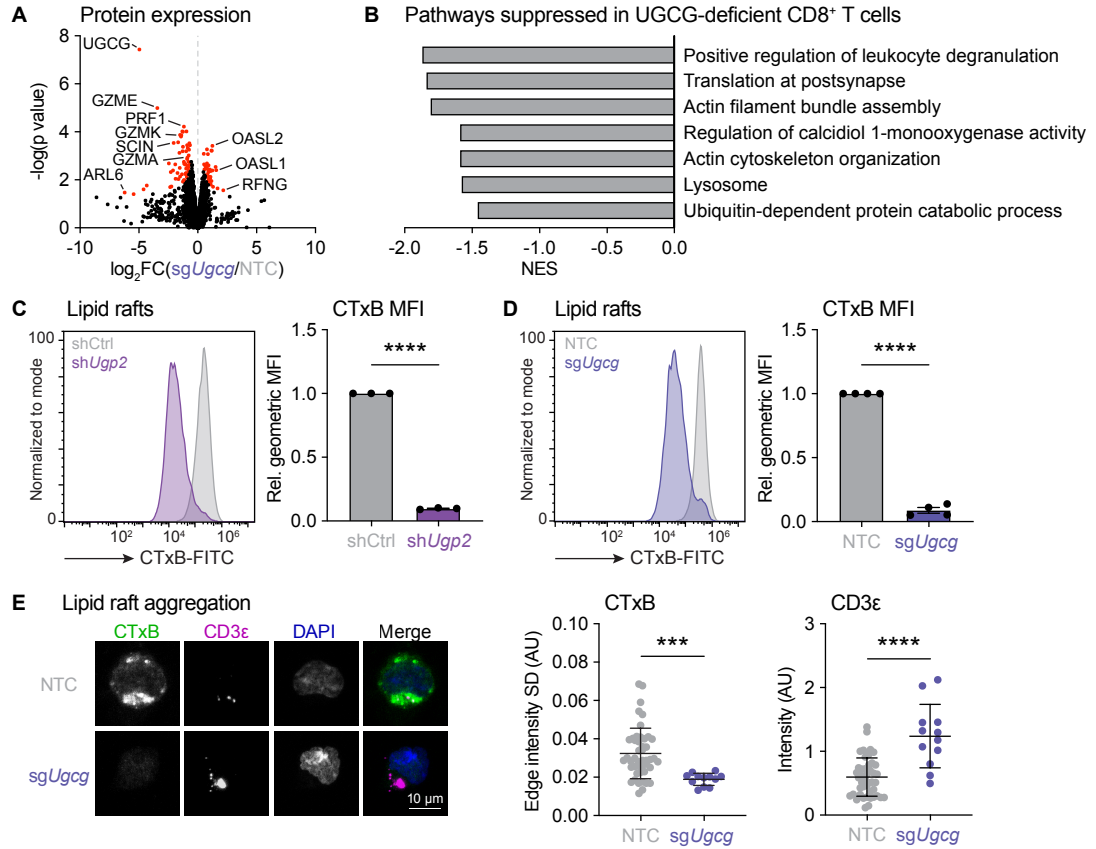
A
Protein expression
UGCG
GZME
PRF1
GZMK
SCIN
GZMA
ARL6
OASL2
OASL1
RFNG
-log(p value)
log2FC(sgUgcg/NTC)
B
Pathways suppressed in UGCG-deficient CD8+ T cells
Positive regulation of leukocyte degranulation
Translation at postsynapse
Actin filament bundle assembly
Regulation of calcidiol 1-monooxygenase activity
Actin cytoskeleton organization
Lysosome
Ubiquitin-dependent protein catabolic process
NES
C
Lipid rafts
shCtrl
shUgp2
Normalized to mode
CTxB-FITC
CTxB MFI
Rel. geometric MFI
****
shCtrl
shUgp2
D
Lipid rafts
NTC
sgUgcg
Normalized to mode
CTxB-FITC
CTxB MFI
Rel. geometric MFI
****
NTC
sgUgcg
E
Lipid raft aggregation
CTxB
CD3ε
DAPI
Merge
NTC
sgUgcg
10 μm
CTxB
Edge intensity SD (AU)
***
NTC
sgUgcg
CD3ε
Intensity (AU)
****
NTC
sgUgcg

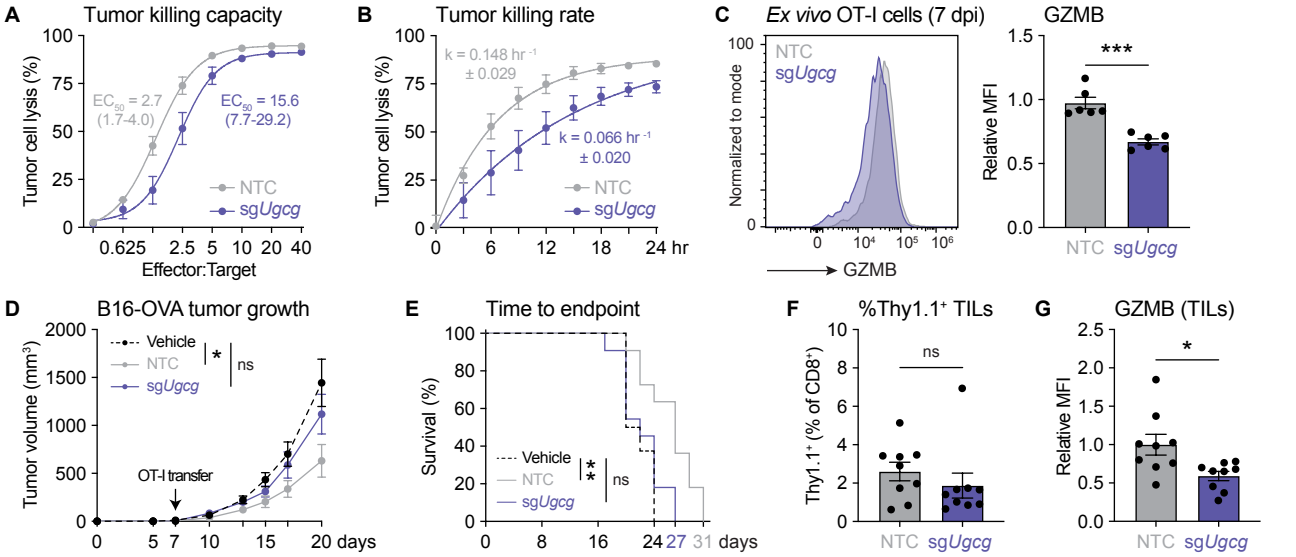
A
Tumor killing capacity
Tumor cell lysis (%)
EC50 = 2.7
(1.7-4.0)
EC50 = 15.6
(7.7-29.2)
NTC
sgUgcg
Effector:Target
B
Tumor killing rate
k = 0.148 hr-1
± 0.029
k = 0.066 hr-1
± 0.020
NTC
sgUgcg
24 hr
C
Ex vivo OT-I cells (7 dpi)
Normalized to mode
NTC
sgUgcg
GZMB
GZMB
Relative MFI
***
NTC
sgUgcg
D
B16-OVA tumor growth
Tumor volume (mm3)
Vehicle
NTC
sgUgcg
*
ns
OT-I transfer
20 days
E
Time to endpoint
Survival (%)
Vehicle
NTC
sgUgcg
**
ns
31 days
F
%Thy1.1+ TILs
Thy1.1+ (% of CD8+)
ns
NTC
sgUgcg
G
GZMB (TILs)
Relative MFI
*
NTC
sgUgcg